AGU PUBLICATIONS

Journal of Advances in Modeling Earth Systems

RESEARCH ARTICLE

10.1002/2016MS000767

Key Points:
- The regime-sorted dynamic changes dominate the thermodynamic changes in terms of the absolute magnitude
- Both the thermodynamic and dynamic changes contribute to positive cloud feedback in the moderate-to-strong subsidence regimes
- Changes in the stability of the convective regimes and the subsidence strength are important for interpreting cloud feedback mechanisms

Correspondence to:
K.-M. Xu,
Kuan-Man.Xu@nasa.gov

Citation:
Xu, K.-M., and A. Cheng (2016), Understanding the tropical cloud feedback from an analysis of the circulation and stability regimes simulated from an upgraded multiscale modeling framework, *J. Adv. Model. Earth Syst.*, *8*, 1825–1846, doi:10.1002/2016MS000767.

Received 27 JUL 2016
Accepted 7 NOV 2016
Accepted article online 15 NOV 2016
Published online 2 DEC 2016

Understanding the tropical cloud feedback from an analysis of the circulation and stability regimes simulated from an upgraded multiscale modeling framework

Kuan-Man Xu[1] and Anning Cheng[2]

[1]Climate Science Branch, NASA Langley Research Center, Hampton, Virginia, USA, [2]EMC/NCEP, NOAA, College Park, Maryland, USA

Abstract As revealed from studies using conventional general circulation models (GCMs), the thermodynamic contribution to the tropical cloud feedback dominates the dynamic contribution, but these models have difficulty in simulating the subsidence regimes in the tropics. In this study, we analyze the tropical cloud feedback from a 2 K sea surface temperature (SST) perturbation experiment performed with a multiscale modeling framework (MMF). The MMF explicitly represents cloud processes using 2-D cloud-resolving models with an advanced higher-order turbulence closure in each atmospheric column of the host GCM. We sort the monthly mean cloud properties and cloud radiative effects according to circulation and stability regimes. We find that the regime-sorted dynamic changes dominate the thermodynamic changes in terms of the absolute magnitude. The dynamic changes in the weak subsidence regimes exhibit strong negative cloud feedback due to increases in shallow cumulus and deep clouds while those in strongly convective and moderate-to-strong subsidence regimes have opposite signs, resulting in a small contribution to cloud feedback. On the other hand, the thermodynamic changes are large due to decreases in stratocumulus clouds in the moderate-to-strong subsidence regimes with small opposite changes in the weak subsidence and strongly convective regimes, resulting in a relatively large contribution to positive cloud feedback. The dynamic and thermodynamic changes contribute equally to positive cloud feedback and are relatively insensitive to stability in the moderate-to-strong subsidence regimes. But they are sensitive to stability changes from the SST increase in convective and weak subsidence regimes. These results have implications for interpreting cloud feedback mechanisms.

1. Introduction

A great challenge for climate projection to increasing concentrations of greenhouse gases is the representation of the effects of clouds in global climate models (GCMs). Model spreads in cloud feedback are still too large to confidently project climate change from greenhouse warming [e.g., *Bony and Dufresne*, 2005; *Soden and Vecchi*, 2011; *Vial et al*., 2013]. This issue is related to the complexity to parameterize the subgrid effects of clouds, convection, precipitation, and radiation in large-scale models or GCMs [*Randall et al*., 2003, 2007]. For example, a change in cloud microphysics representation of convective clouds in a single GCM can alter the equilibrium climate sensitivity that spans the full range of all conventional GCMs with parameterized physical processes [*Zhao et al*., 2016]. *Zhao et al*. [2016] found that model differences resulting from different representations of the conversion from condensate to convective precipitation are dominated by shortwave feedbacks and contributed to by the broad circulation regimes ranging from large-scale ascent to subsidence.

Differing from conventional GCMs, the multiscale modeling framework (MMF) approach proposed by *Grabowski* [2001] and *Khairoutdinov and Randall* [2001] explicitly simulates the largest and most organized circulations within deep convective systems using a cloud-system resolving model (CRM) within each grid column of the host GCM. MMF is also able to simulate low clouds successfully when it is incorporated with a higher-order turbulence closure in its CRM component [*Cheng and Xu*, 2011, 2013a, 2013b; *Xu and Cheng*, 2013a, 2013b; *Painemal et al*., 2015]. Physical processes such as turbulence, cloud dynamics, cloud microphysics and radiation represented in such an MMF interact at the CRM grid scales. Parameterizations are still needed within CRMs but they are treated at much smaller temporal and spatial scales than in GCMs. Thus,

the interactions among these physical processes at smaller scales enable the improvement of the overall simulation of present-day climate [e.g., *Khairoutdinov et al*., 2005; *Xu and Cheng*, 2013a, 2013b] and an improved simulation of climate changes in idealized experiments and coupled ocean-atmosphere experiments [*Wyant et al*., 2006a; *Arnold et al*., 2014; *Stan and Xu*, 2014; *Bretherton et al*., 2014, hereafter B14].

The earlier climate change simulations with an MMF known as Super-parameterized Community Atmosphere Model (SPCAM) [*Wyant et al*., 2006a] produced rather weak equilibrium climate sensitivity. With a +2 K sea surface temperature (SST) experiment [*Cess et al*., 1990, 1996], *Wyant et al*. [2006a] found that the climate sensitivity parameter (λ) was 0.41 K W^{-1} m^2, which was much lower than an observationally based estimate of the lower-bound equilibrium climate sensitivity with constant aerosol forcing for 1970–2010 (0.54 ± 0.14 K W^{-1} m^2) by *Bengtsson and Schwartz* [2013] and the present study (0.53 K W^{-1} m^2). The equilibrium CO_2 doubling temperatures are 1.5 K (SPCAM), 2.0 ± 0.5 K [*Bengtsson and Schwartz*, 2013] and 2.0 K (this study), assuming a CO_2 doubling forcing of 3.7 W m^{-2} [*Myhre et al*., 1998]. With an updated SPCAM and a longer model integration of +4 K SST experiment, B14 obtained a λ value of 0.58 K W^{-1} m^2. This increase of climate sensitivity is due to an increase of shallow cumulus in the control simulation with present-day SST and sea ice concentration relative to *Wyant et al*. [2006a] and a decrease of shallow cumulus in the perturbed climate instead of an increase of shallow cumulus in *Wyant et al*. [2006a]. In a coupled run with quadrupled CO_2 concentration, *Stan and Xu* [2014] and B14 found that an equilibrium climate sensitivity to CO_2 doubling is 2.77°C, which is again lower than the median of the conventional GCMs (3.1–3.3°C) but within the full range of 2.0–5.7°C of 31 GCMs [*Ringer et al*., 2014; *Mauritsen and Stevens*, 2015]. The inadequate simulation of stratocumulus clouds on the west coasts of continents contributes to the lack of positive cloud feedback in SPCAM. On the other hand, stratocumulus clouds are well simulated in SPCAM when a higher-order turbulence closure is incorporated in its CRM component [*Cheng and Xu*, 2011]. The simulated stratocumulus clouds are further improved with a higher vertical resolution in the low troposphere [*Xu and Cheng*, 2013a].

Cloud radiative feedbacks can directly impact the climate sensitivity and the internal variability of the climate system; for example, a negative cloud feedback lowers the equilibrium climate sensitivity and acts to reduce the internal variability. How do these feedbacks operate in the real atmosphere and models as climate changes? There are several basic types of cloud radiative feedback mechanisms. One is related to the change in cloud distributions [e.g., *Schneider*, 1972; *Wetherald and Manabe*, 1980]; a decrease in cloud fraction decreases both shortwave radiative cooling and longwave radiative warming. For low clouds, shortwave cooling dominates longwave warming and thus the net cloud feedback is mostly due to shortwave cloud feedback. The cloud distribution feedback also includes the change in cloud temperature or altitude. Another type of feedback is due to the change in cloud optical depth, τ [*Paltridge*, 1980]. A warm climate increases in-cloud condensate, which is supported by in situ observations [*Feigelson*, 1978]. This cloud feedback is negative for liquid clouds because optically thicker clouds reflect more shortwave radiation, but its sign is less certain for ice clouds. Other feedbacks involve changes in cloud microphysical properties such as particle radius and ice diameters, phase, and cloud geometry [e.g., *Colman et al*., 2001].

In general, cloud radiative feedback is defined as the change in a cloud process associated with radiative fluctuation of a climate state. This definition means that cloud radiative feedback is not simply a globally averaged quantity. It varies spatially and temporally and is mostly influenced by large-scale circulation and thermodynamic changes. One step toward unraveling the complex cloud feedback lies ultimately in understanding the influence of the large-scale atmospheric circulation on clouds [*Stephens*, 2005] . To isolate the changes in cloud process, the changes in cloud and radiative quantities can be sorted by circulation regimes, as first proposed by *Bony et al*. [2004]. This approach used the large-scale pressure velocity at 500 hPa as a measure of circulation regimes. The cloud/radiative property changes for a circulation regime between two climate states are effectively expressed as those due to changes in large-scale dynamics and those due to changes in thermodynamics (nondynamics). In addition to correctly simulating the changes in the frequency of occurrence of circulation regimes and cloud/radiative properties between the two climate states, the frequency of occurrence of the circulation regimes and the regime-mean cloud/radiative properties of the present-day climate are important. Further details of this approach will be discussed in section 3.3.

In addition to the sorting approach of circulation regimes, stability regimes will also be jointly used in the present study [*Eitzen et al*., 2011; *Myers and Norris*, 2013; *Medeiros et al*., 2015] to effectively isolate the two major cloud-reduction mechanisms for low clouds, the stability and the dynamic mechanisms. For

stratocumulus cloud response, a stability reduction reduces cloud fraction due to an increase in cloud top entrainment [*Wood and Bretherton*, 2006] while the dynamical mechanism in terms of a reduction in the large-scale subsidence allows a deep inversion with more vertically developed clouds [*Myers and Norris*, 2013]. This sorting approach of two parameters does not provide a direct constraint on the thermodynamic mechanism [*Qu et al*., 2015], due to the inversion humidity change, and the radiative mechanism, due to the vertical moisture transport change in response to reduced radiative cooling in the free atmosphere [*Christensen et al*., 2013].

The primary objective of this study is to dissect the tropical cloud feedback from the perspective of sorting the circulation and stability regimes simulated from an upgraded MMF. MMF cannot realistically simulate boundary layer clouds without a realistic treatment of much smaller-scale turbulent eddies. As stated earlier, understanding low-cloud responses to climate change is a priority due to the large spread of climate sensitivity in conventional GCMs. A higher-order turbulence closure has been implemented and tested in MMFs to improve low-cloud simulations. *Cheng and Xu* [2011] upgraded the embedded CRM with an intermediately prognostic higher-order turbulence closure (IPHOC) [*Cheng et al*., 2004; *Cheng and Xu*, 2006] to SPCAM. They showed a greatly improved simulation of low-level clouds over the tropical and subtropical oceans despite the very coarse horizontal resolution used in the host GCM. Using a finite-volume $1.9^\circ \times 2.5^\circ$ dynamical core for the host GCM with an increase in the vertical resolution below 700 hPa, *Xu and Cheng* [2013a, 2013b], *Cheng and Xu* [2013a, 2013b], and *Painemal et al*. [2015] examined the climatology, seasonal cycle, diurnal cycle, and cloud regime transition. This model can produce a global-mean and annual-mean low cloud amount that is within 5.3% of active/passive sensor merged observations (50.3%) [*Kato et al*., 2011]. The seasonal variations of low clouds in the eastern Pacific are comparable to and in some instances better than those produced by the best regional high-resolution climate models [*Wyant et al*., 2010; *Wang et al*., 2011]. The cloud regime transition from stratocumulus and shallow cumulus to deep convective clouds and the diurnal cycle of the low clouds are realistic. In contrast, global low cloud amount distributions were only slightly improved in an MMF with the Cloud Layer Unified by Binormals [*Golaz et al*., 2002] higher-order closure and more sophisticated aerosol and microphysics parameterizations [*Wang et al*., 2015].

Since the computational expense of the IPHOC version of SPCAM (hereafter, SPCAM-IPHOC) is roughly 400-fold higher than that of a conventional GCM with the same grid resolution as that of its host GCM, it is practical to perform some limited climate change simulations by focusing on climate changes that can be analyzed using simulations of just a few years, for example, the $+2$ K SST perturbation experiment [*Cess et al*., 1990, 1996] and the abrupt CO_2 increase experiment [*Hansen et al*., 1984]. The earliest climate-change simulations with MMF also had durations of a few years [*Wyant et al*., 2006a, 2012] although B14 recently performed 35 year integrations. The differences in the results between *Wyant et al*. [2006a, 2012] and B14 were attributed to two different versions of SPCAM rather than the different durations of the integrations.

The rest of the paper is organized as follows. Section 2 provides a brief description of the model and the numerical experiments. Results of the basic features of the MMF sensitivity experiment and the detailed cloud feedback analyses are presented in section 3. Summary and discussions are given in section 4.

2. Model Description and Experiment Design

A detailed description of the SPCAM-IPHOC MMF can be found in *Cheng and Xu* [2011] and *Xu and Cheng* [2013a]. The MMF consists of a host GCM and an embedded 2-D CRM in each atmospheric grid column of the GCM. The host GCM is the Community Atmosphere Model, version 3.5 (CAM3.5), with the finite-volume dynamical core [*Collins et al*., 2006]. The earlier version of SPCAM-IPHOC used CAM version 3.5 with the semi-Langragian dynamical core as the host GCM and the horizontal and vertical resolutions of the host GCM were coarser [*Cheng and Xu*, 2011]. In either study, the CRM is the System for Atmospheric Modeling (SAM) [*Khairoutdinov and Randall*, 2001] that was upgraded with IPHOC to better represent planetary boundary layers (PBLs) and low clouds in place of the low-order turbulence closure in the standard SAM. The details of IPHOC are given in *Cheng and Xu* [2006, 2008, 2011], but will be briefly described later.

Convective and stratiform precipitation processes, usually parameterized in a conventional GCM, are resolved explicitly (but crudely) on the CRM fine grid cells, with 32 CRM grid columns and 4 km of horizontal grid spacing. The CRM time step is 10 s. Cloud microphysics and radiation are parameterized within the CRM. Tendencies of heat and moisture from the CRM scale communicate to the large scale via the GCM.

The dynamical core provides the large-scale advective tendencies to the CRMs at the larger GCM time step [*Khairoutdinov and Randall*, 2001]. The surface turbulence fluxes over land grid points are calculated from a land surface model in CAM3.5 and are provided to the CRMs. Those over ocean grid points are calculated on the GCM grids from the prescribed SSTs.

The sub-CRM-grid dynamic and thermodynamic variability is parameterized by a higher-order turbulence closure (IPHOC) to provide a consistent treatment of turbulent transport and subgrid-scale (SGS) condensation. IPHOC assumes a joint double-Gaussian distribution of liquid water potential temperature, total water, and vertical velocity [*Cheng and Xu*, 2006]. The properties of the double-Gaussian probability density function (PDF) such as the means, variances, and skewnesses are determined from the first-order, second-order, and third-order moments of the variables given above using a few assumptions because there are more Gaussian properties than the total number of the input moments. The details of the derivation can be found in *Cheng and Xu* [2006, 2011]. The PDF is used to diagnose cloud fraction and grid-mean liquid water mixing ratio, as well as the buoyancy terms and fourth-order terms in the equations describing the evolution of the second-order and third-order moments. Although the SGS distribution of condensate, such as ice and cloud water, is known, microphysical conversion and rainwater collection rates are calculated from the grid-mean properties. *Cheng and Xu* [2009] performed an off-line CRM testing of a consistent formulation of SGS microphysical processes, which was not implemented in the MMF presented in this study.

The details of the control experiment design were given in *Xu and Cheng* [2013a]. Briefly, the MMF was forced by specifying climatological SST and sea ice distributions (Hadley Centre Sea Ice and Sea Surface Temperature data set (HadISST)) [*Rayner et al*., 2003] with monthly mean annual cycles. That is, there is no imposed interannual variability. The GCM has a horizontal grid size of $1.9^\circ \times 2.5^\circ$ and there are 32 layers in the vertical with 12 layers below 700 hPa. The extra six layers below 700 hPa are used to better resolve the structures of stratocumulus clouds, compared to the standard CAM3.5 and SPCAM configurations. The embedded CRMs have the same vertical levels as the host GCM. The simulation was integrated for 10 years and 3 months. The results from the last 9 years are analyzed in this study.

The sensitivity experiment simulates the climate sensitivity to an SST increase. The SSTs are uniformly increased by 2 K over oceanic grid points (hereafter, this experiment is referred to as +2 K). The rest of the experiment design is identical to the control described above. The land surface temperatures are allowed to vary during the integration. This type of experiment, though highly idealized, is useful to examine climate sensitivity and cloud feedback for a prescribed climate change [*Cess et al*., 1990, 1996]. It is called an "inverse" climate change experiment because the climate change is prescribed and the models produce radiative imbalance at the top of the atmosphere (TOA), which is used to estimate climate sensitivity and cloud feedback. There have been a number of studies using such an experiment design with conventional GCMs [e.g., *Bony et al*., 2004; *Ringer et al*., 2006, 2014; *Wyant et al*., 2006b; *Demoto et al*., 2013] and MMFs [e.g., *Wyant et al*., 2006a; B14] since *Cess et al*. [1990, 1996] pioneered this type of experiment. This design was included as part of the Fifth Phase of the Coupled Model Intercomparison Project (CMIP5) [*Taylor et al*., 2012]. *Wyant et al*. [2006a] performed a similar +2 K experiment with an earlier version of SPCAM using CAM3.0 with the semi-Langragian dynamical core as the host GCM. B14 used a newer version of SPCAM to perform an experiment with +4 K SST. As in the present study, B14 used CAM3.5 with the finite-volume dynamical core as the host GCM. Additionally, it should be pointed out that the TOA radiative energy balance of the control experiment with SPCAM-IPHOC is within the uncertainty of the measurements [*Xu and Cheng*, 2013a].

3. Results

3.1. Changes in the Thermodynamics and Circulation

The land surface temperature responds to radiative forcing changes induced by SST increases. This response is not spatially uniform over all continents due to varying changes in circulation. Its magnitudes range from 0.5 to 4.0 K (Figure 1a). Most of the increases are above 2 K except for the west and midlatitude/high-latitude part of the Eurasia continent centered at (50°E, 60°N) and a few small areas near the coasts of East America and East Asia and the Antarctic. The largest warming occurs over Alaska/west Canada, Brazil, India, South and East Africa as well as on the equatorward side of Australia. These regional variations are

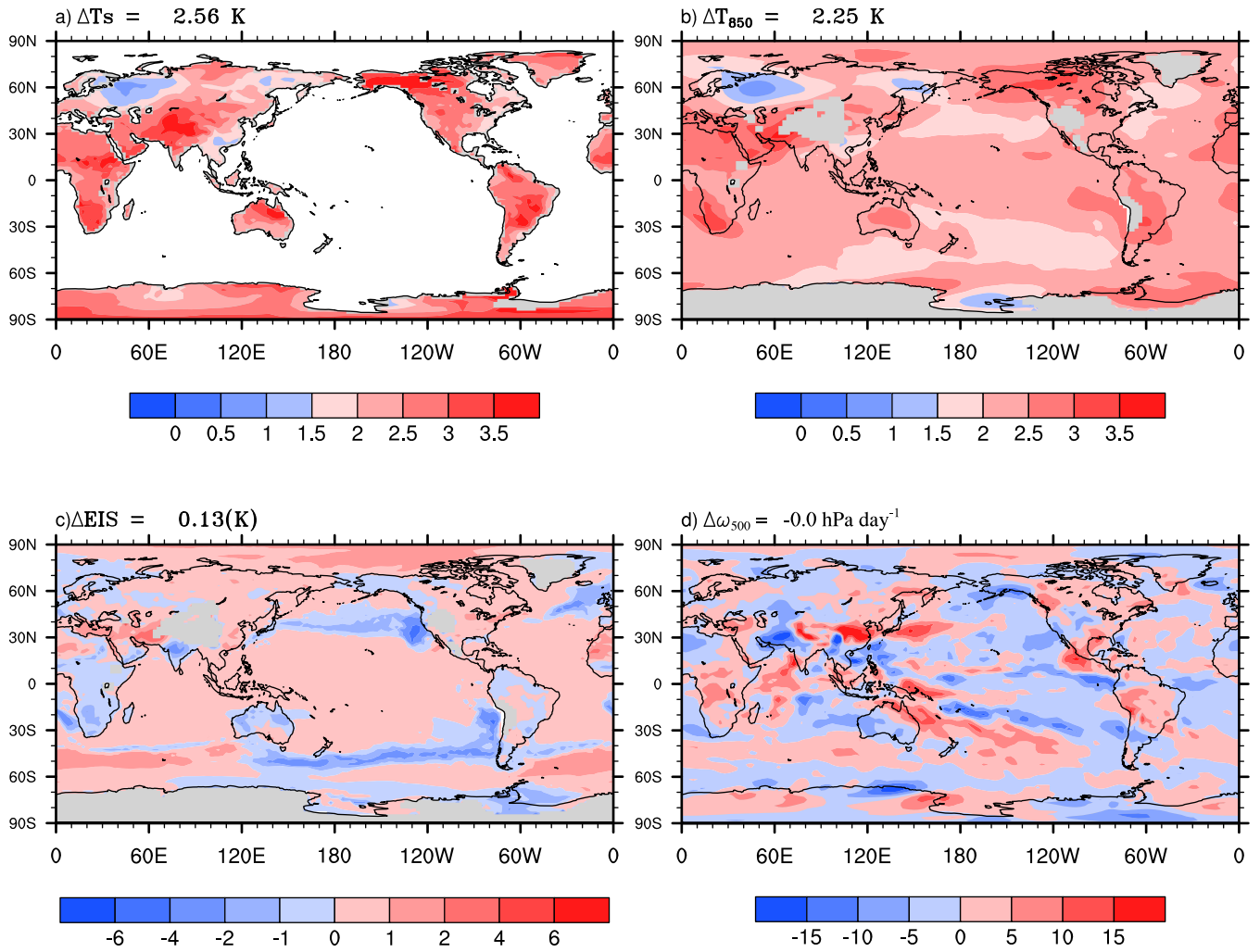

Figure 1. Global distributions of the differences in temperature at (a) surface, (b) 850 hPa, (c) estimated inversion strength, and (d) pressure velocity at 500 hPa between +2 K SST and control experiments. In Figure 1a, only the differences over lands are plotted.

due to the differences in surface characteristics and/or topography that are coupled with variable circulation changes.

The land surface warming also impacts the atmosphere above. The temperature change at 850 hPa is consistent with that of surface temperature (Figure 1b). The tropospheric temperature change above the continents is relatively less than the change in surface temperature (Figure 1a). This is also the case over the midlatitude storm track regions, where the polarward movement of the midlatitude storms increases the cooling equatorward, which is related to less infrared warming resulting from reduced cloud amount. Parts of the west coasts of South and North America/Africa are, however, relatively warmer at 850 hPa than the surface, which is related to the decrease of stratocumulus clouds off the coasts, as discussed later.

To further illustrate the change in the thermodynamic properties, the Estimated Inversion Strength (EIS), which provides an estimate of the strength of the PBL inversion and is a cloud-regime-independent measure of low tropospheric stability [*Wood and Bretherton*, 2006], is shown in Figure 1c. It is apparent that EIS decreases significantly over several oceanic basins off the coasts where stratocumulus clouds reside, in particular, the southeast (SE) and northeast (NE) Pacific and SE Atlantic, as well as the equatorward of the storm track regions. On the other hand, EIS increases slightly in the vast region of the tropics and subtropics away from the coasts albeit with small magnitude, as well as the polarward of the storm track regions.

Table 1. Tropical Means of Selected Variables for the Control Experiments in B14 and This Study, and Tropical-Mean (30°S–30°N) and Global-Mean Changes of the Sensitivity Experiments (+4 K SST in B14 and +2 K SST in This Study) From Their Respective Control Experiments[a]

	Tropical Mean, Control		Tropical Mean Change		Global Mean Change	
	B14	This Study	B14	This Study	B14	This Study
Surface temperature (K)	298.65	298.42	2.27	2.20	2.30	2.21
ω_{500} (hPa d^{-1})	−0.85	−0.46	−0.26	−0.35	−0.01	−0.01
Low cloud (%)	31.31	37.54	−0.31	0.09	0.02	0.15
Middle cloud (%)	10.79	9.26	−1.05	−1.04	−1.26	−0.97
High cloud (%)	28.49	39.12	−0.12	−1.08	0.44	−0.07
Total cloud (%)	52.19	61.01	−0.36	−0.64	−0.05	−0.09
Liquid water path (mm)	103.73	100.69	2.86	3.92	6.60	7.00
Ice water path (mm)	38.70	37.63	−1.22	−1.06	−1.47	−1.31
SW CRE (W m^{-2})	−75.19	−51.80	0.95	0.35	−0.33	−0.39
LW CRE (W m^{-2})	36.81	24.95	−0.44	−0.27	0.08	0.23
Net CRE (W m^{-2})	−38.38	−26.85	0.51	0.08	−0.25	−0.16

[a]The changes from B14 are scaled by a factor of 2.

As discussed earlier, the large-scale circulations are expected to change from the control to +2 K experiments. The differences in large-scale pressure velocity at 500 hPa (ω) between the two experiments are used to measure these changes (Figure 1d). The regional patterns in the ω differences are generally similar to B14. The most significant difference from B14 is the larger decreases in the subsidence strengths in the stratocumulus regions near the coasts of continents, for example, the SE and NE Pacific, SE Atlantic, and west coast of Australia. Statistically, there is a smaller difference in the tropical mean ω change between the land and ocean in the present study. These tropical mean ω values (after scaled to +2 K from B14) are +1.34 hPa d^{-1} (land) and −0.81 hPa d^{-1} (ocean) in B14, compared to +0.85 hPa d^{-1} (land) and −0.78 hPa d^{-1} (ocean) in the present study. See Table 1 for comparisons of the tropical-mean and global-mean statistics of other selected variables.

3.2. Cloud Response and Changes in Cloud Radiative Effects

The global-mean and annual-mean low cloud fraction increases slightly (0.15%) for the +2 K experiment (Figure 2a), which is similar to the +4 K experiment (0.04%) with SPCAM in B14 (Table 1). In MMF, the low clouds are defined as those with their cloud top pressures greater than 700 hPa. Cloud fraction is obtained from a CRM column using the maximum overlap and then horizontally averaged over the CRM domain. As seen from Figure 2a, the local changes in low cloud fraction are large (±8%). The largest changes occur in the storm track regions of the control experiment, with decreases over the 30° and 50° belts in both hemispheres and increases over the polarward of 50°. This major feature is related to the polarward movement of the storm tracks as SST increases. In the tropics and subtropics, there are significant increases in low cloud fraction over the shallow cumulus regions located far away from the coasts but significant decreases over the stratocumulus regions off the coasts, for example, the NE Pacific.

The low cloud fraction averaged over the 30°S–30°N belt changes little between the two experiments (Table 1). The decrease in stratocumulus cloud fraction is associated with the decrease in EIS off the coasts (Figure 1e). In the shallow and deep convective regions over the open oceans, low clouds increase as opposed to decrease in B14. This contributes to the tropical-mean reduction in B14 (Table 1). The stability increases over these regions (Figure 1c) may explain these increases, which will be further discussed in section 3.4.

The annual-mean middle clouds, which are defined as those with cloud top pressures between 700 and 400 hPa, and high clouds, which correspond to those with cloud top pressures less than 400 hPa, show decreases over most parts of the tropics/subtropics except for the regions impacted by the movement of SPCZ and ITCZ (Figures 2c and 2e). The reductions in middle, high, and total cloud fractions between 30°S and 30°N (0.01–0.02) are also shown in the zonal mean whereas the zonal-mean low cloud fraction changes by less than 0.005 (Figure 3a). These results are similar to B14 except for a smaller reduction in low cloud fraction.

The cloud radiative effects (CREs) are defined as the differences in TOA radiative flux between the clear sky and all sky [*Ramanathan et al.*, 1989]. As the vertical structures of clouds and cloud liquid water content (LWC) change, CREs are expected to change accordingly (Table 1). In general, the LW CRE changes are related mostly to changes in middle/high clouds while the SW CRE changes are associated primarily with

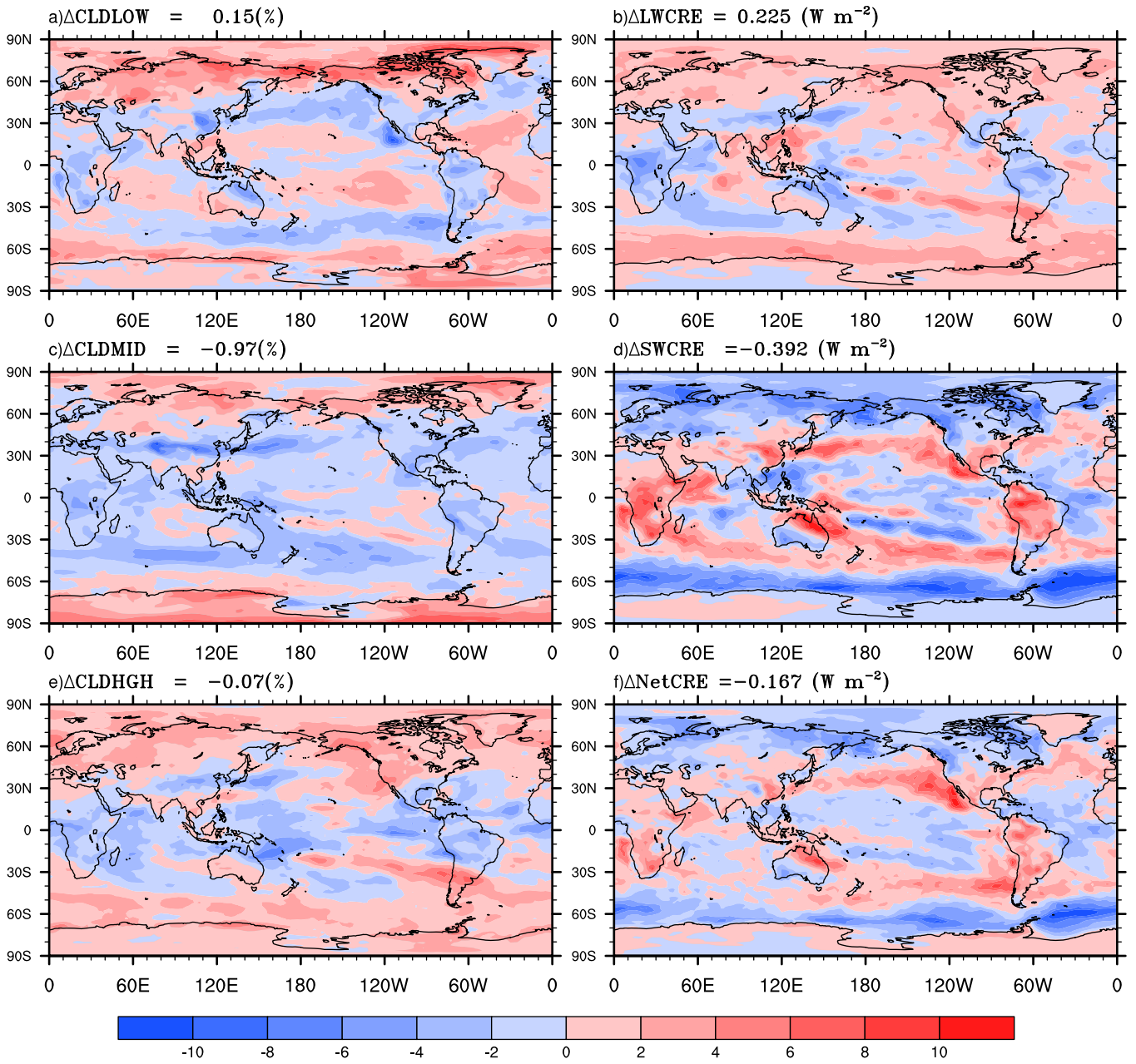

Figure 2. Global distributions of the differences in (a) low, (c) middle, and (e) high cloud fractions and (b) longwave, (d) shortwave, and (f) net cloud radiative effects (CREs) between the +2 K and control experiments. Unit for cloud fraction is %, while unit for CRE is W m^{-2}.

(negative) changes in low clouds (Figures 2b and 2d). The net CRE changes reflect mostly those of the SW CRE (Figure 2f). These results are supported by the spatial correlation between the CREs and cloud fractions at various levels (Table 2). High cloud fractions have the highest correlation with the LW CRE (0.74), while low cloud fractions have the highest negative correlations with the SW and net CREs.

For the tropical regions, the magnitudes of the CRE changes are smaller than those in the midlatitude/high latitude (Figures 2b, 2d, and 2f), which are also seen from the zonal means (Figure 3c). Both the large cloud liquid water path (LWP) increase (Figure 3b) and cloud fraction changes contribute to the large CRE changes in the midlatitude/high latitude, which are related to the polarward movement of storm tracks. The increase in SW CRE in the tropical and subtropical regions corresponds well to the decrease of low clouds, for example, off the coasts of SE and NE Pacific and over the lands of South Africa and America (Figure 2d). Over the deep convective regions such as the tropical western Pacific, Indian Ocean, and western Atlantic, the

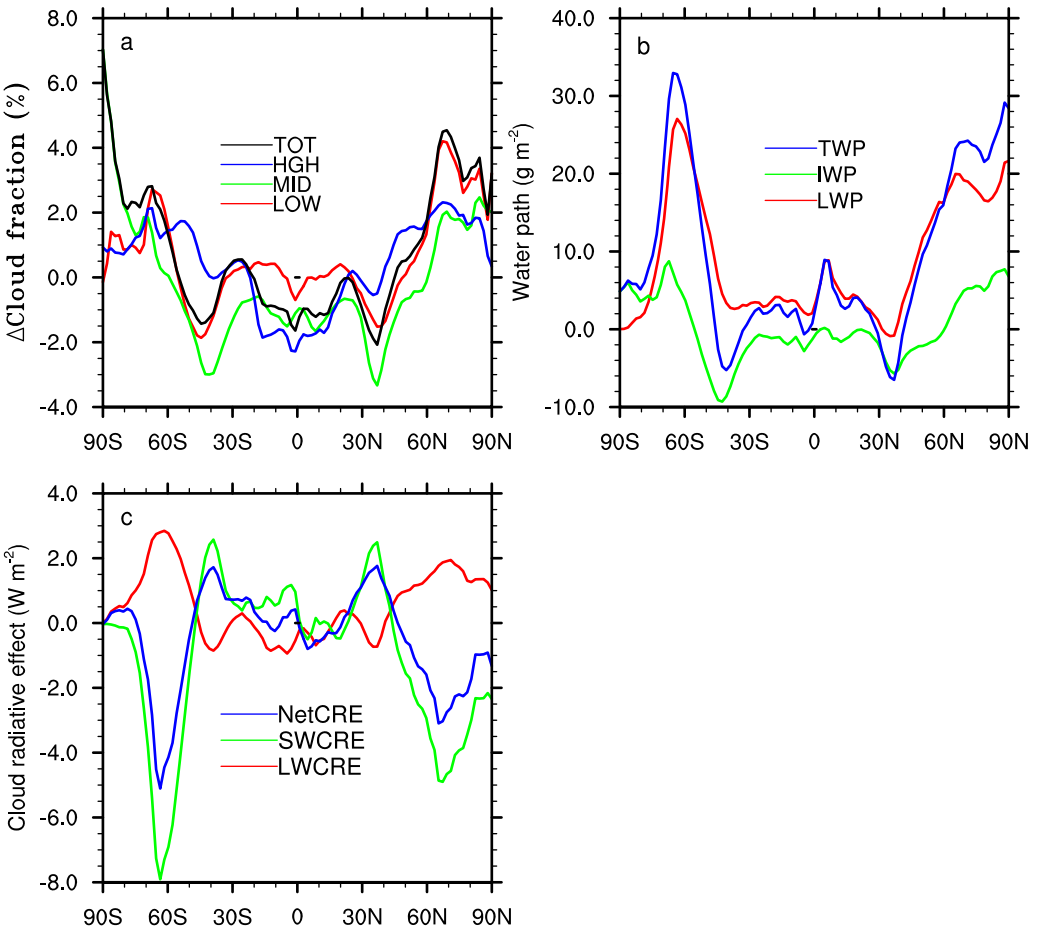

Figure 3. Annual and zonal mean changes in (a) low, middle, high, and total cloud fraction, (b) cloud liquid, ice, and liquid + ice (total) water paths, and (c) shortwave, longwave, and net cloud radiative effects between the +2 K and control experiments.

increases in SW CRE are accompanied by the decreases in LW CRE, resulting in small changes in the net CRE over most of the tropics where low clouds do not dominate. It is important to point out that the LWC changes (not shown) also contribute to the CRE changes, which can be identified in the SE Pacific where low cloud fractions decrease slightly but the SW CRE increases significantly.

3.3. The Circulation Regime Analysis

The circulation regime analysis of cloud feedback was first proposed by *Bony et al.* [2004] to isolate the cloud variability associated with changes in the large-scale circulations from that associated with changes in the nondynamics (thermodynamics) as climate changes. The circulation regimes are represented by the large-scale monthly mean vertical velocity at 500 hPa; i.e., the pressure velocity (ω). Following the notations in *Bony et al.* [2004], the circulation regimes are discretized at a prescribed interval (for example, at 10 hPa d^{-1}). The PDF of ω satisfies the following condition in the continuous form:

$$\int_{-\infty}^{+\infty} P(\omega)d\omega=1. \quad (1)$$

Here P is the statistical weight of each circulation regime or the relative area covered by each regime. Let $\bar{C}$ denote a domain-averaged and time-averaged value of C, where C can be a variable representing a cloud property or CRE. The domain is

Table 2. Correlation Coefficients Between the Changes in Cloud Radiative Effects (CREs) and Low, Middle, and High Cloud Fractions Between the +2 K and Control Experiments

	ΔLOW	ΔMID	ΔHIGH
ΔSW CRE	−0.66	−0.41	−0.48
ΔLW CRE	0.42	0.51	0.74
ΔNet CRE	−0.64	0.22	−0.15

typically chosen as the entire Tropics (30°S and 30°N). The time average is typically over a multiple year period of the experiments. So,

$$\bar{C} = \int_{-\infty}^{+\infty} P(\omega) C(\omega) d\omega. \quad (2)$$

Let δC denote the change of C from the control to sensitivity experiment. The domain-averaged and time-averaged change is $\overline{\delta C}$. We can differentiate (2), which yields three terms

$$\overline{\delta C} = \int_{-\infty}^{+\infty} C(\omega)\delta P(\omega) d\omega + \int_{-\infty}^{+\infty} P(\omega)\delta C(\omega) d\omega + \int_{-\infty}^{+\infty} \delta P(\omega)\delta C(\omega) d\omega. \quad (3)$$

The first term on the right-hand side (RHS) of (3) is related to the contribution from changes in the circulation regimes, that is, changes in the statistical weight of each regime multiplied by the mean property of each regime in the control experiment. The second term is related to the contribution from changes in the cloud properties such as cloud height, cloud fraction, and radiative flux within a given regime between the two experiments, weighted by the statistical weight of each regime. This term measures the changes in the thermodynamics (nondynamics). The last term is related to the covariation of the dynamic and thermodynamic changes. This term is typically 1 order of magnitude smaller than the first two terms.

Previous studies used dynamic and thermodynamic components to describe the first two terms on the RHS of (3), respectively [*Bony et al.*, 2004; *Vial et al.* 2013]. *Bony and Dufresne* [2005], *Vial et al.* [2013], *Medeiros et al.* [2015], and *Zhao et al.* [2016] used this sorting approach to understand cloud feedback and its differences between the low and high climate sensitivity models. In this study, we distinguish the terms without integration from those with integration over the entire range of circulation regimes. We will use the dynamic and thermodynamic "changes" when those [$C(\omega)\delta P(\omega)$, $P(\omega)\delta C(\omega)$] associated with an individual regime are discussed. But we will use the dynamic and thermodynamic "contributions" when the tropical-mean changes are discussed; i.e., integrated over the entire range of circulation regimes. For example, the dynamic contribution may be small due to shifts of the statistical weight of individual regimes with small differences in cloud property between regimes but the dynamic change can be large for individual regimes because of the population shifts between the adjacent bins. Thus, the amplitude of the dynamic change can be overestimated compared to that when the population of a given bin remains unchanged. This caution has not been taken in previous studies [*Bony et al.*, 2004; *Clement and Soden*, 2005; *Yukimoto et al.*, 2006; *Yuan et al.*, 2008; *Medeiros et al.*, 2008, 2015; *Vial et al.*, 2013], but should be kept in mind when these changes are compared.

Before discussing the changes of cloud properties and CREs [$\delta C(\omega)$] from the control to sensitivity experiments, it is critically important to examine the ω PDF and its change (Figures 4a and 4d) because conventional GCMs show large intermodel differences in the ω PDF [*Wang and Su*, 2013]. As mentioned earlier, we are most interested in the tropical cloud feedback. Thus, we use the monthly averaged grid point data over the 30°–30°N belt from the last nine years of both experiments. Although the ω PDF over the land grid points is different from that over the oceanic grid points (Figure 4a), the ω PDFs for the oceanic and all areas are similar due to the small tropical land fraction. Therefore, both the land and oceanic grid points are combined in this study. The bin interval for ω is 10 hPa d^{-1}.

The ω PDF shows a skewed distribution with a peak at ~20 hPa d^{-1}, which corresponds to the subsidence rate of free tropospheric air constrained by the clear-sky radiation cooling of ~2 K d^{-1}. Most of the tropics belongs to the weak and moderate subsidence regimes with ω between 0 and 40 hPa d^{-1} (Figure 4a). The exact cutoff ω values for different regimes will be given shortly. This result indicates the predominance of the weak subsidence regimes in contributing to the tropical cloud feedback [*Vial et al.*, 2013]. The shape of the PDF resembles that of the ensemble mean PDF of CMIP5 models and the PDF of reanalysis data [e.g., *Bony et al.*, 2004; *Wang and Su*, 2013]. However, some of the individual CMIP5 models underestimate the power for the weak subsidence regimes and overestimate the power for the weakly convective regimes compared to the reanalysis data [*Wang and Su*, 2013] and the present result. Figure 4a also shows that the power decreases rapidly toward the stronger subsidence regimes ($\omega > 30$ hPa d^{-1}), compared to the decreasing rate of the strongly convective regimes ($\omega < -30$ hPa d^{-1}). That is, the strong subsidence regimes occur less frequently than the strongly convective regimes at the same magnitude of ω. The uptick at -90 hPa d^{-1} is due to an artifact of bin cutoff, but these large ω are associated with overactive convection in the western Pacific, a common feature in MMFs [*Khairoutdinov et al.*, 2005; *Cheng and Xu*, 2014].

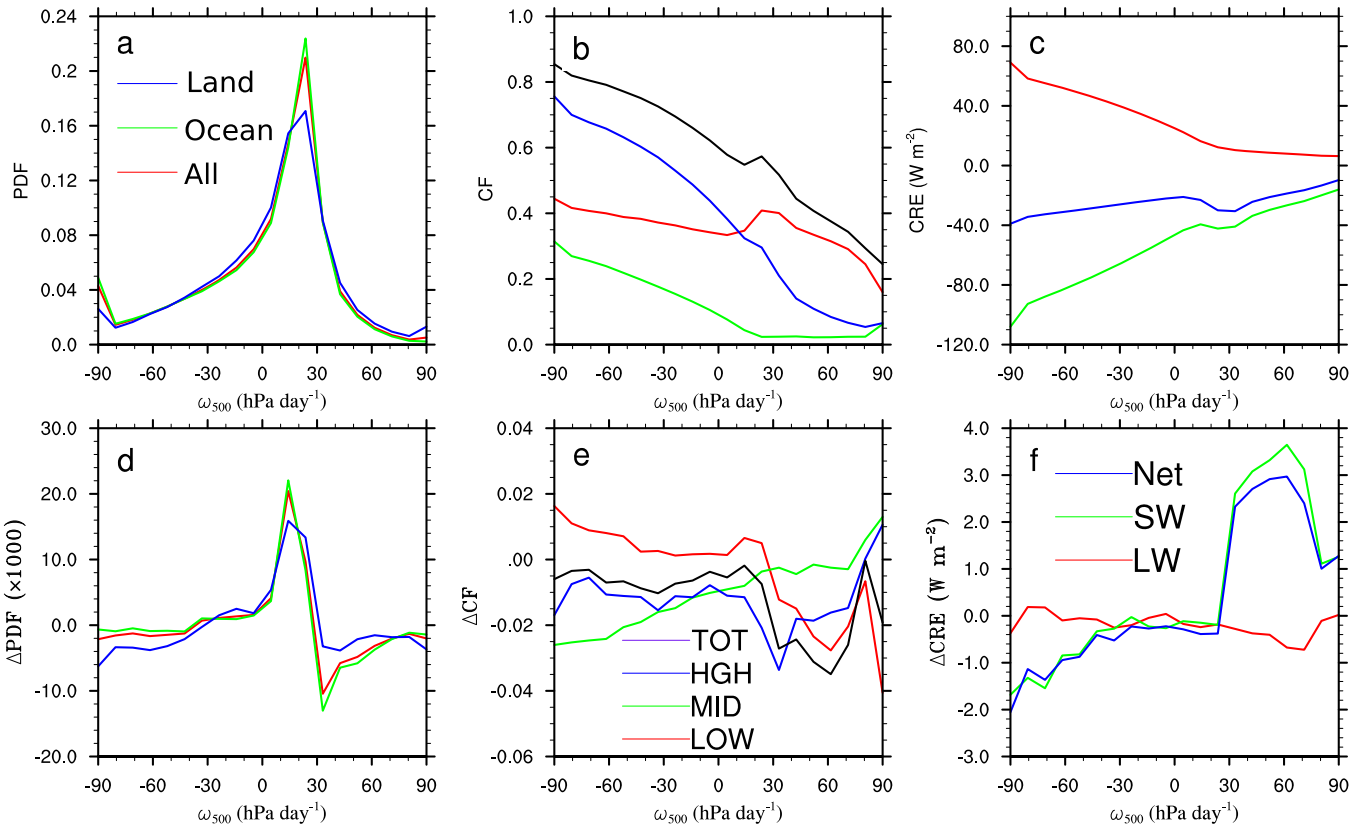

Figure 4. (a) The frequency of occurrence of midtropospheric pressure velocity (ω_{500}) over the tropics, and (d) the difference of PDF between the +2 K SST and control experiments. (b) The mean total, low, middle, and high cloud fractions and (c) the mean shortwave, longwave, and net cloud radiative effects and (e, f) their respective changes between the +2 K SST and control experiments sorted by monthly ω_{500}.

Figure 4d shows that the largest change in the ω PDF occurs in subsidence regimes with ω between 0 and 40 hPa d^{-1}. The magnitude of the changes is about 10% of the ω power of the control experiment. The increases in the ω power in the weak subsidence regimes are mostly at the expense of stronger subsidence regimes due to reduced clear-sky radiation cooling resulting from the moister free troposphere. The strongly convective regimes are also slightly less frequent. This result, which will be further discussed later, is typically referred to as the slowdown of the tropical circulations [e.g., *Vecchi and Soden*, 2007; *He and Soden*, 2015]. This aspect of the MMF results is, thus, qualitatively consistent with CMIP5 models.

Based upon the sign of $\Delta P(\omega)$ (Figure 4d) and value of ω, we divide the entire range of circulation regimes into four subranges: strongly convective ($\omega < -35$ hPa d^{-1}), weakly convective ($0 > \omega > -35$ hPa d^{-1}), weak subsidence ($0 < \omega < 25$ hPa d^{-1}), and moderate-to-strong subsidence ($\omega > 25$ hPa d^{-1}), similar to *Medeiros et al.* [2008]. It is expected that shifting of population (i.e., statistical weight) within each subrange can contribute to cloud property changes more than shifting of population at the edge of these subranges can because the changes in ω at most locations between the two experiments are less than 10 hPa d^{-1} (Figure 1d), the size of individual ω bins. These distinct subranges can, therefore, be physically more meaningful than an individual bin for comparing the dynamic and thermodynamic changes.

The variations of the mean cloud fractions and SW, LW, and net CREs of the control experiment as a function of circulation regimes are shown in Figures 4b and 4c. These properties within the same ω bin are averaged. Figure 4b shows that low, middle, high, and total cloud fractions decrease as ω increases except that low/total cloud fraction has a secondary peak (bump) at 20 hPa d^{-1}. The high cloud fraction at −90 hPa d^{-1} is at 0.75. It decreases as ω increases and levels off at ∼0.05 at 80 hPa d^{-1}. This agrees well with the Cloud-Aerosol Lidar and Infrared Pathfinder Satellite Observations (CALIPSO) analysis presented in *Wang and Su* [2013], but it is noted that the simulated cloud fractions are defined differently. Additionally, high and low cloud fractions are comparable (∼0.40) in the weak subsidence regimes, implying for the

coexistence of shallow and deep convection there. Their rates of decrease with increasing ω there are lower than those of either the convective or strong subsidence regimes.

The variations of the mean SW, LW, and net CREs with ω are generally consistent with the Clouds and the Earth's Energy System (CERES) [*Wielicki et al*., 1996] observations [*Wang and Su*, 2013] except for a slightly larger increasing rate in the SW and net CREs with ω in the subsidence regimes (Figure 4c). These differences have only small impact on the calculation of the dynamic contribution discussed later ($\leq$ 0.03 W m^{-2}) if one replaces the MMF CREs by the CERES observations. The SW cooling effect of clouds is larger than the LW heating effect, resulting in a small net cooling effect for all the circulation regimes. Their amplitudes decrease as ω increases, due primarily to the decrease of total cloud fraction with increasing ω.

The changes in cloud fractions and CREs between the experiments are mostly less than 10% of the means of the control experiment (Figures 4e and 4f). The mean quantities are calculated for each experiment and then the differences between the two experiments are taken for the same ω bin. For cloud fractions, the most significant change is the decrease of low and total clouds (0.01–0.04) in the moderate-to-strong subsidence regimes, which exceeds 10% of the means. This suggests for potentially positive feedbacks due to the decreases in cloud fractions.

The most significant changes in CREs between the experiments are the large increase (up to 3.5 W m^{-2}) in the SW and net CREs in the moderate-to-strong subsidence regimes (Figure 4f). The reduction in low cloud fraction in the $+2$ K experiment is the primary reason (Figure 4e). The CRE increases are usually simulated in the high-sensitivity conventional GCMs but there is a large model spread [*Bony and Dufresne*, 2005; *Vial et al*., 2013]. In the strongly convective regimes, both the SW and net CRE changes are negative, with a magnitude of up to 2 W m^{-2}. The slight increases in low cloud fraction cannot explain this result, but its combination with the increase in total cloud liquid + ice water path (TWP) can, as shown later.

Next, we will examine the dynamic and thermodynamic changes (Figure 5) and contributions (Table 3). In agreeing with studies using conventional GCMs [e.g., *Bony et al*., 2004; *Vial et al*., 2013], the thermodynamic contribution dominates the dynamic contribution for cloud fraction, LWP (and TWP), i.e., a factor of, at least, 3 larger. The magnitudes of both the dynamic and thermodynamic contributions are more comparable for cloud ice water path (IWP) and all CREs although the thermodynamic contributions for SW and LW CREs are still larger than the dynamic ones. Because of the similar mean values of cloud properties in the weak subsidence regime (Figures 4b and 4c) and the large population shift resulting in changes with opposite signs, the integrated dynamic changes over the entire tropics are expected to be small. On the other hand, the property changes in the relatively small areas with active convection and strong subsidence provide the thermodynamic contribution. It is noted that the dynamic contributions in all variables listed in Table 3 except for LWP and low and middle cloud fractions represent a significant portion of the total contributions, having the same sign for all CREs and IWP but opposite signs for high and total cloud fractions and TWP. These results suggest that the dynamic contribution can be important to understand cloud feedback, which was mostly ignored in some studies [e.g., *Zhao et al*., 2016].

To further explain the dynamic contribution, we represent cloud fractions/CREs as a linear function of ω as in *Wyant et al*. [2006b]; i.e., $C(\omega) = C_0 + C_1\omega$, where C_0 and C_1 are obtained from Figures 4b and 4c using either a simple linear or a piecewise linear fit. The estimates of the dynamic contributions from a simple linear fit have an opposite sign in CREs and middle cloud fraction compared to the direct calculation (Table 4). The piecewise linear fit with only two to four segments improves the agreement with the direct calculation in both sign and magnitude. This result implies for a direct link between the dynamic contribution and the large-scale circulation.

Before discussing Figure 5, it should be pointed out that the vertical scales in the dynamic change (Figures 5a, 5c, and 5e) are much larger than those in the thermodynamic change (Figures 5b, 5d, and 5f). As expected, the variations of $\Delta P(\omega)$ (Figure 4d) determine those of the dynamic changes in cloud properties and CREs with ω; that is, the sign between -35 and $+25$ hPa d^{-1} range is opposite to that on either side of this range. The peaks (with opposite signs) are centered at 15 and 35 hPa d^{-1}, respectively. The cancellation resulting from opposite signs explains the small magnitudes of the dynamic contributions (Table 3). The dynamic changes in the weak subsidence regime are related to strong negative cloud feedback (Figure 5c) due to the increases in both cloud fractions, IWP and LWP (Figures 5a and 5e). Note that the change of LWP/LWP includes that of cloud fraction. On the other hand, the dynamic changes in the moderate-to-

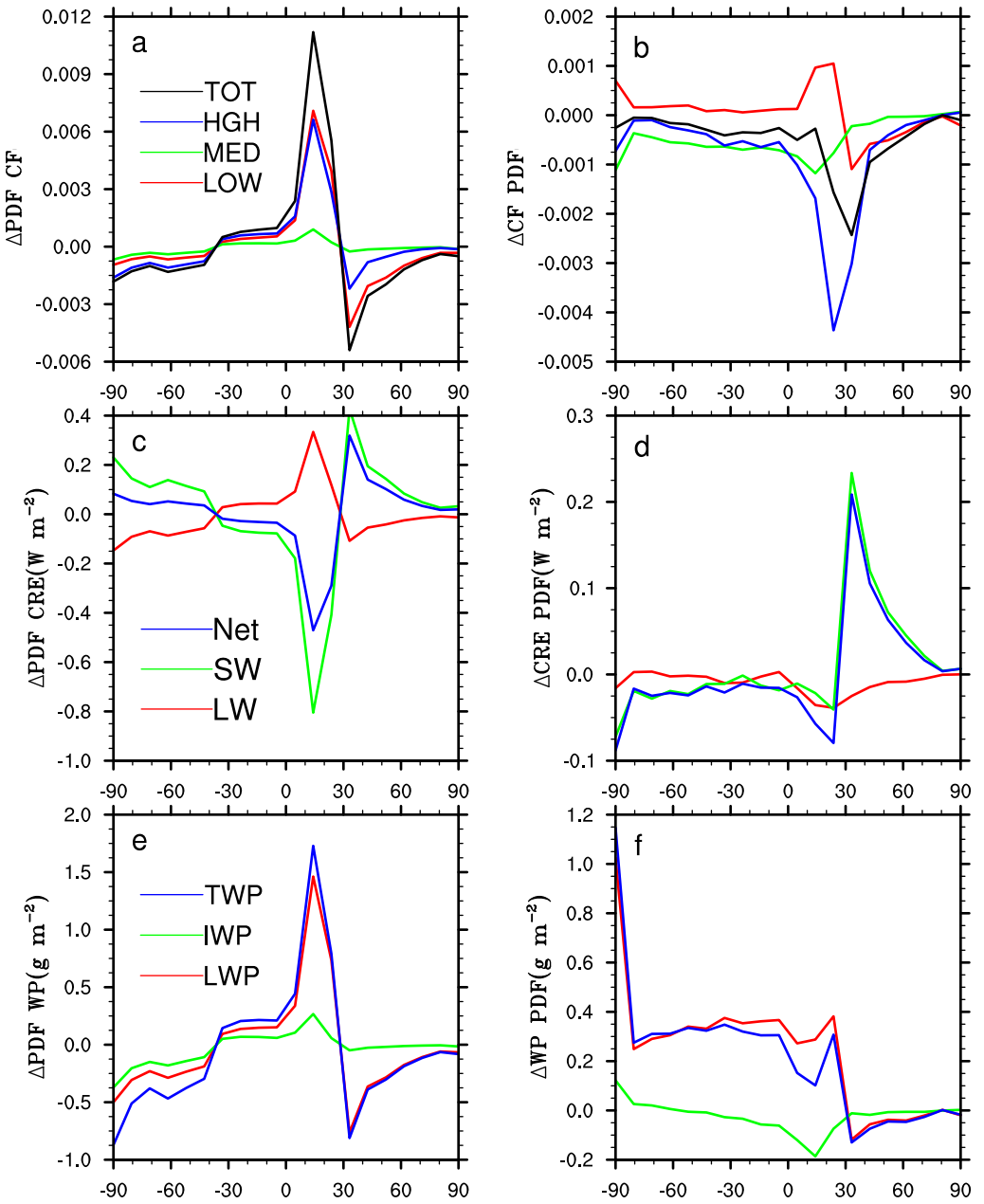

Figure 5. The (a, c, e) dynamic and (b, d, f) thermodynamic changes in (a, b) cloud fractions, (c, d) shortwave, longwave, and net cloud radiative effects, and (e, f) cloud liquid water path (LWP), cloud liquid ice path (IWP), and their sum (TWP) as a function of midtropospheric pressure velocity (ω_{500}).

strong subsidence regimes are related to positive cloud feedback due to the decreases in both low cloud fraction and LWP, which are more than twice as large as that for the strongly convective regimes. This difference in magnitude is due to a stronger cancellation between LW and SW CREs for deep than shallow convection and stratocumulus (Figure 5c).

The magnitudes of the thermodynamic change in CREs for the moderate-to-strong subsidence regimes are slightly smaller than those of the dynamic change there (Figures 5c and 5d), which is related to relatively smaller decreases in low cloud fraction and negligible decreases in LWP. For the weak subsidence regimes, the increases in LWP and low cloud fraction (Figures 5a and 5f) counterbalance the effects of the decreases in middle, high and total cloud fractions (Figure 5b), resulting in negative cloud feedback. In the convective regimes, the thermodynamic change in LW CRE is nearly zero and that of all CREs changes little with ω

Table 3. The Dynamic and Thermodynamic Contributions to Cloud Property and CRE Changes and Their Sum Integrated Over the Entire Range of Circulation Regimes, Following Equation (3)

	Dynamic	Thermodynamic	Sum
Low cloud fraction (%)	0.00	0.09	0.09
Middle cloud fraction (%)	−0.05	−0.99	−1.04
High cloud fraction (%)	0.46	−1.55	−1.09
Total cloud fraction (%)	0.25	−0.89	−0.64
Cloud liquid water path (mm)	−0.49	4.41	3.92
Cloud ice water path (mm)	−0.60	−0.46	−1.06
Cloud total water path (mm)	−1.09	3.95	2.86
SW CRE (W m^{-2})	0.13	0.21	0.34
LW CRE (W m^{-2})	−0.09	−0.19	−0.28
Net CRE (W m^{-2})	0.04	0.03	0.07

except for nearly −90 hPa d^{-1}, due to a slight cancellation in the effects between the LWP/TWP increase and the (middle and high) cloud fraction decreases. The negative cloud optical depth feedback due to LWP increases (coupled with small cloud fraction change) (Figure 5e) operates in the strongly convective regimes. Thus, the key for understanding the tropical cloud feedback should be focused on the change in the SW CRE in the subsidence regions as far as the sorting approach of circulation regimes is concerned, agreeing with the results of the high-sensitivity subset of conventional GCMs [e.g., *Vial et al*., 2013] but contrasting with *Zhao et al*. [2016] which emphasizes the convective regimes. Conventional GCMs have to improve the simulation of stratocumulus clouds and the transition between shallow and deep convection in the weak subsidence regimes in order to capture this critical element of the tropical cloud feedback.

3.4. The Joint Circulation-Stability Regime Analysis

In the present study, we introduce a second parameter, EIS [*Wood and Bretherton*, 2006], to represent the "stability" regimes although they are intertwined with the circulation regimes. A positive EIS corresponds to a stable regime while a negative EIS corresponds to an unstable regime. There is a good correspondence between the stability and circulation regimes for strongly convective and strong subsidence regimes [*Medeiros et al*., 2015]. We use the ω-EIS pair, as in *Eitzen et al*. [2011], *Myers and Norris* [2013], and *Medeiros et al*. [2015], to classify the joint circulation-stability regimes. With the addition of EIS as the second parameter, equations (1)–(3) can be modified with an additional integral and a second variable (EIS). We will use the "dynamic change" $[C(\omega, EIS)\times\delta P(\omega, EIS)]$ and "thermodynamic change" $[P(\omega, EIS)\times\delta C(\omega, EIS)]$, respectively, to describe the first two terms on RHS of equation (3), except for the joint ω–EIS regimes.

Statistical significance levels (90, 95, and 99%) are used to identify where the joint ω-EIS regimes undergo the most significant changes in a cloud property $[\delta C(\omega, EIS)]$ from the control to sensitivity experiments. The significance level is determined according to the two-sample *t* test [*Wilks*, 2006], which uses the mean and standard deviation of the changes in a cloud property between the two experiments. As in the analysis presented in section 3.3, the monthly mean data over the 30°S to 30°N belt are used.

Next, we will examine the frequency of occurrence of the joint circulation-stability (ω-EIS) regimes. In this analysis, a circulation regime is further partitioned into different stability regimes with an EIS bin size of 1.33 K. The range of ω is reduced from −90 to +90 hPa d^{-1} (Figure 4a) to −60 to +60 hPa d^{-1} because of the lack of data in some EIS bins for strongly convective and strong subsidence regimes. The size of ω bin increases to 13.33 hPa d^{-1}. The center value of a bin is used to plot Figure 6. For the bins on the four edges of the plots, data outside the bin ranges are included.

Table 4. The Dynamic Contributions to Cloud Fraction and CRE Changes From a Direct Calculation Using Equation (3), and Estimates From a Simple Linear or Piecewise Linear Relationship Between Cloud Property and Large-Scale Pressure Velocity at 500 hPa (ω) of the Control Simulation

	Direct	Simple Linear	Piecewise Linear
Low cloud fraction (%)	0.00	0.65	0.01
Middle cloud fraction (%)	−0.05	0.55	−1.31
High cloud fraction (%)	0.46	1.30	0.91
Total cloud fraction (%)	0.25	1.43	1.25
SW CRE (W m^{-2})	0.13	−1.79	0.88
LW CRE (W m^{-2})	−0.09	1.20	−0.71
Net CRE (W m^{-2})	0.04	−0.57	0.02

As shown in Figure 6a, the joint PDF has the strongest power in the weak subsidence regimes ($\omega = 20$ hPa d^{-1}) with weak stability ($-0.7\ \text{K} < \text{EIS} < 2.0$ K). In general, the PDF power shifts toward more unstable (stable) regimes as the ascending (descending) motion increases except for two edges of the histogram due to bin cutoffs. One has the stabilities of 0.6 to −4 K for $\omega = -60$ hPa d^{-1} bin, and another has the subsidence of 0–40 hPa d^{-1} for EIS = 8 K bin. The change in the

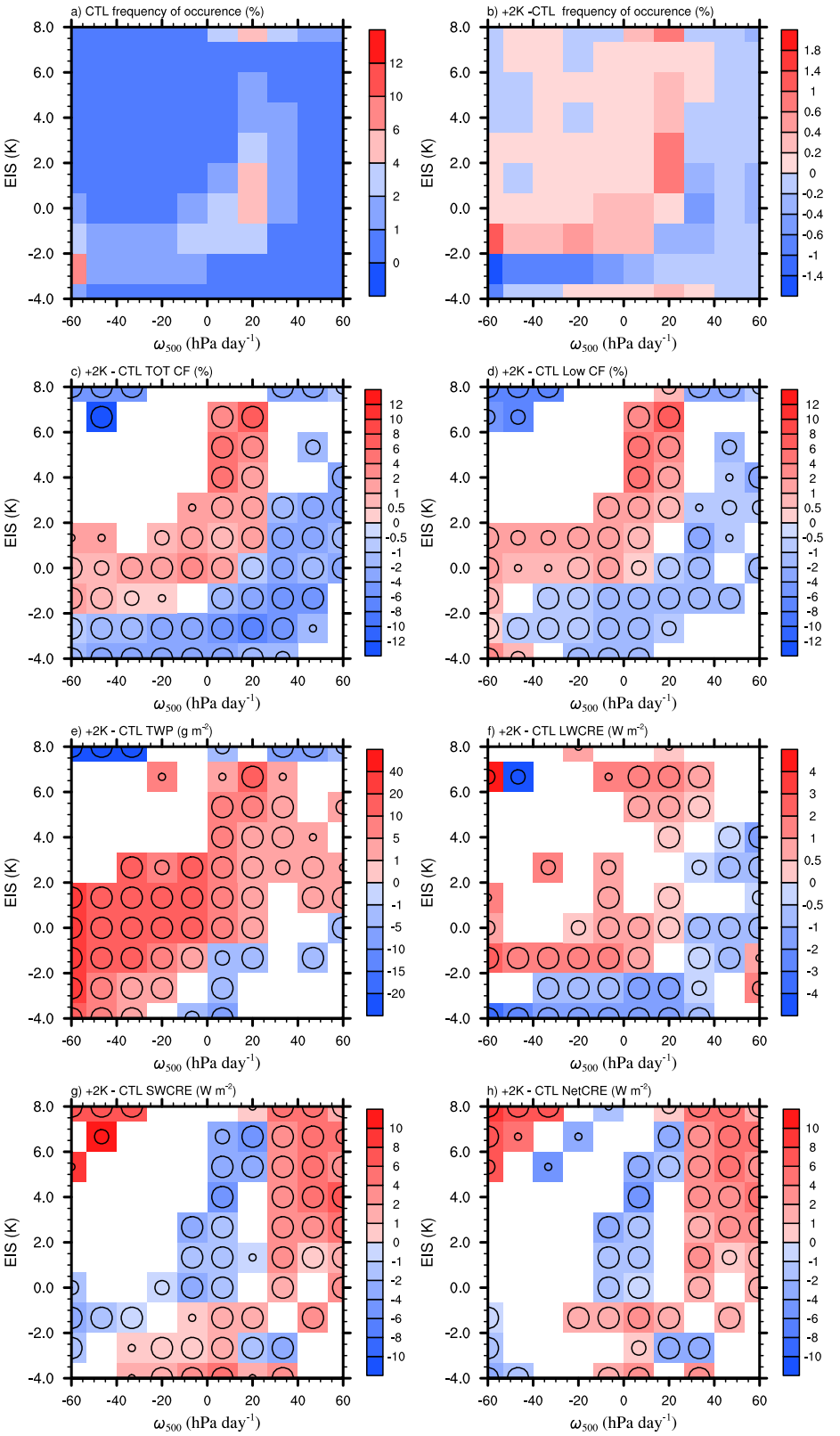

Figure 6. (a) Joint ω-EIS frequency of occurrence for the control experiment, and (b) the difference between the +2 K and control experiments. The mean changes in (c) total and (d) low cloud fractions, (e) cloud liquid + ice water path (TWP), (f) longwave, (g) shortwave, and (h) net cloud radiative effects between the +2 K and control experiments sorted by EIS and ω. (c–h) Statistical significant levels in the mean changes are indicated by the different sizes of circles (large, 99%; medium, 95%; and small, 90%).

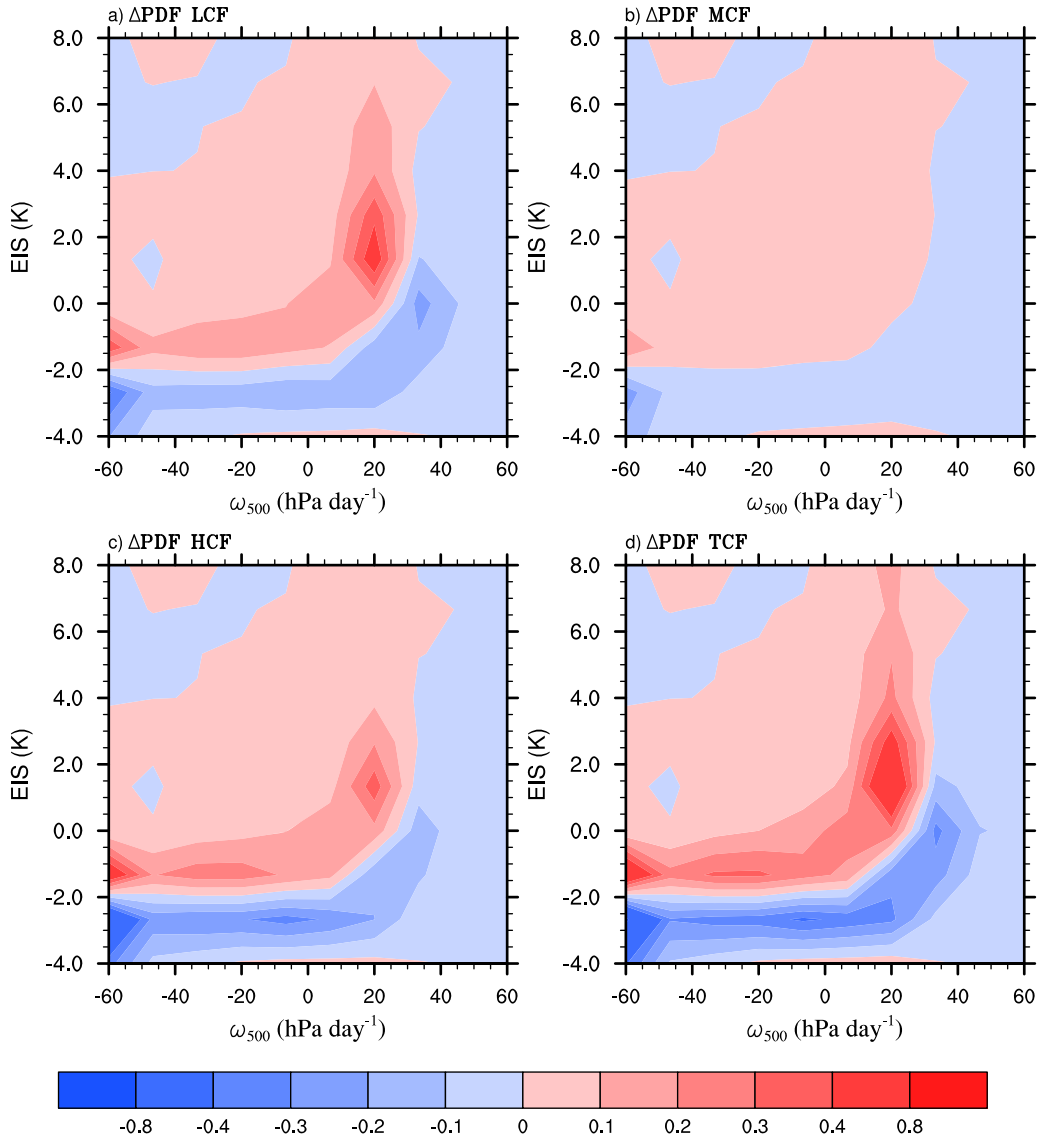

Figure 7. The dynamic changes in (a) low, (b) middle, (c) high, and (d) total cloud fraction as a function of estimate inversion strength (EIS) and large-scale pressure velocity (ω) between the +2 K SST and control experiments. Unit is %.

ω-EIS PDF between the two experiments exhibits shifts of power toward the weaker subsidence regimes for the entire EIS range and toward the more stable stability in the convective to weak subsidence regimes as SST increases (Figure 6b). The transition lines, where the absolute value of the change of power on either side is the largest, occur at EIS $= -2$ K (for $\omega < 13$ hPa d^{-1}) and $\omega = 27$ hPa d^{-1} (for -0.7 K $<$ EIS < 4.7 K), respectively.

The mean changes in total cloud fraction between the experiments (Figure 6c) largely mirror the changes in the power of the ω–EIS PDF (Figure 6b). Significant cloud fraction increases (decreases) are associated with the ω-EIS regimes with large PDF power increases (decreases). For example, there are significant cloud fraction decreases in the subsidence regimes (for EIS up to 3.3 K) and the convective regimes (for EIS < -2 K). In the former regimes, the net CRE increases significantly but also for EISs higher than 3.3 K (Figure 6h). In the latter regimes, the net CRE change is not always significant because it depends on the relative strength of cloud fraction feedback (positive; Figure 6c) and cloud optical depth feedback (negative; Figure 6e).

To a great extent, the mean changes of low cloud fraction mirror those of total cloud fraction (Figure 6d) except for the subsidence regimes at reduced significant levels. The decrease in low cloud fraction for the strong subsidence regimes is moderately significant with a magnitude of about 0.01 for 2 K SST increase,

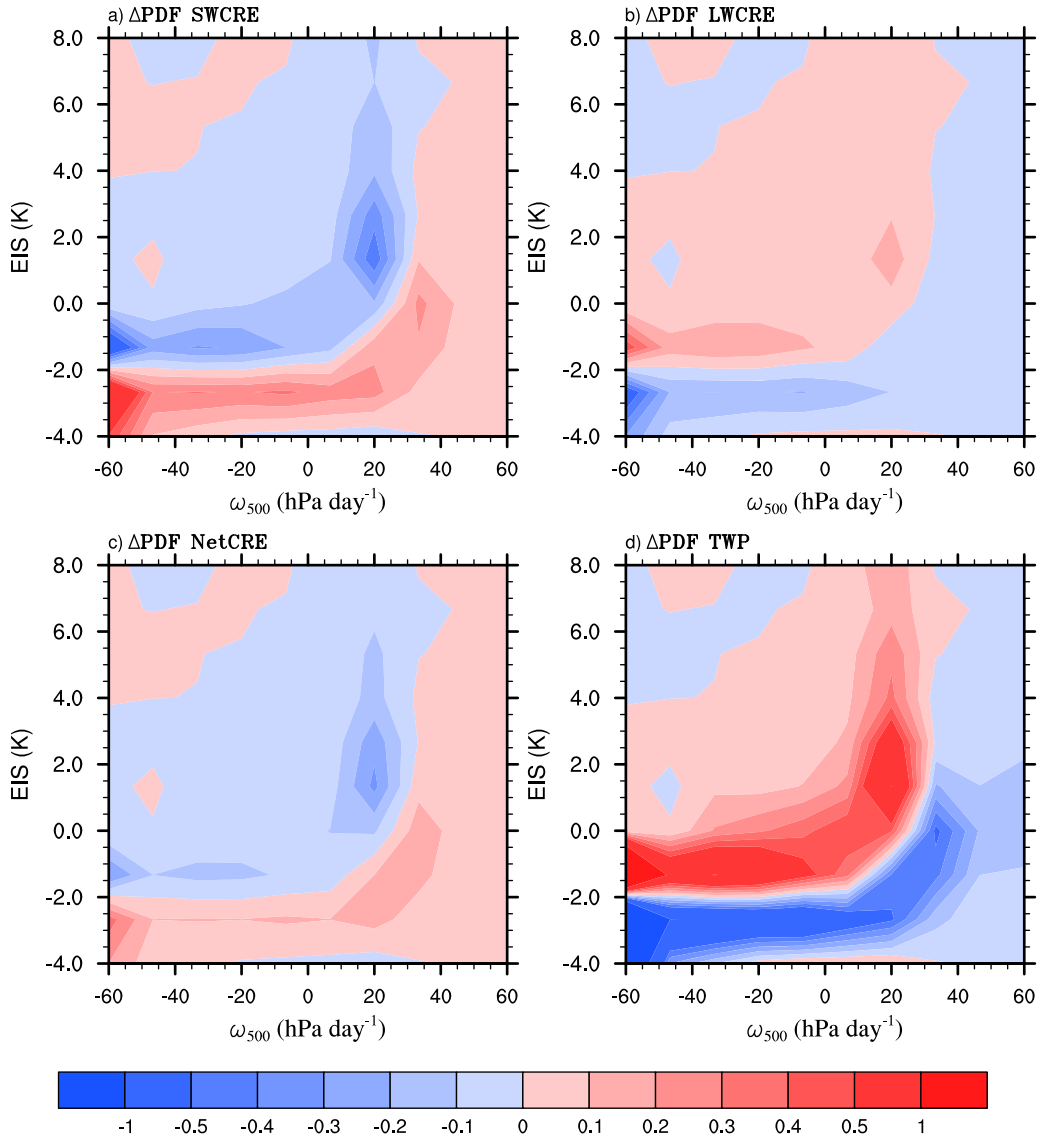

Figure 8. Same as in Figure 7 except for the dynamic changes in (a) shortwave, (b) longwave, and (c) net cloud radiative effect (CRE) and (d) cloud liquid + ice water path (TWP). The color bar for Figure 8d is twice as large. Unit is W m^{-2} for Figures 8a–8c but mm multiplied by 5 for Figure 8d.

which is much lower than that simulated from idealized large-eddy simulations [*Xu et al.*, 2010; *Blossey et al.*, 2013; *Bretherton et al.*, 2013] or of observational analyses [*Qu et al.*, 2014] to support the thermodynamic mechanism [*Qu et al.*, 2015]. The more significant decreases in total cloud fraction for these regimes suggest that decreases in high cloud fraction (not shown, but can be inferred from Figure 9c) are also important to the net CRE increase (Figure 4e). On the other hand, there are significant TWP increases over the majority of the ω–EIS regimes with larger increases in the convective regimes than in the subsidence regimes (Figure 6e). They reduce the magnitude of the net CRE increases due to the decreases in cloud fraction, especially over the convective regimes.

The LW CRE changes (Figure 6f) largely mirror those of total cloud fraction, but with fewer ω-EIS pairs that have significant changes, which may be due to the saturation of cloud emissivity in a warmer climate. The magnitudes of the LW CRE changes are much smaller than those of the SW CRE, by a factor of 2 (Figure 6g). Consequently, the net CRE changes (Figure 6h) are similar to those of the SW CRE.

By analogy with Figure 5, which shows the dynamic and thermodynamic changes in cloud properties and CREs for the circulation regimes, the similar dynamic changes (Figures 7, 8) and thermodynamic changes

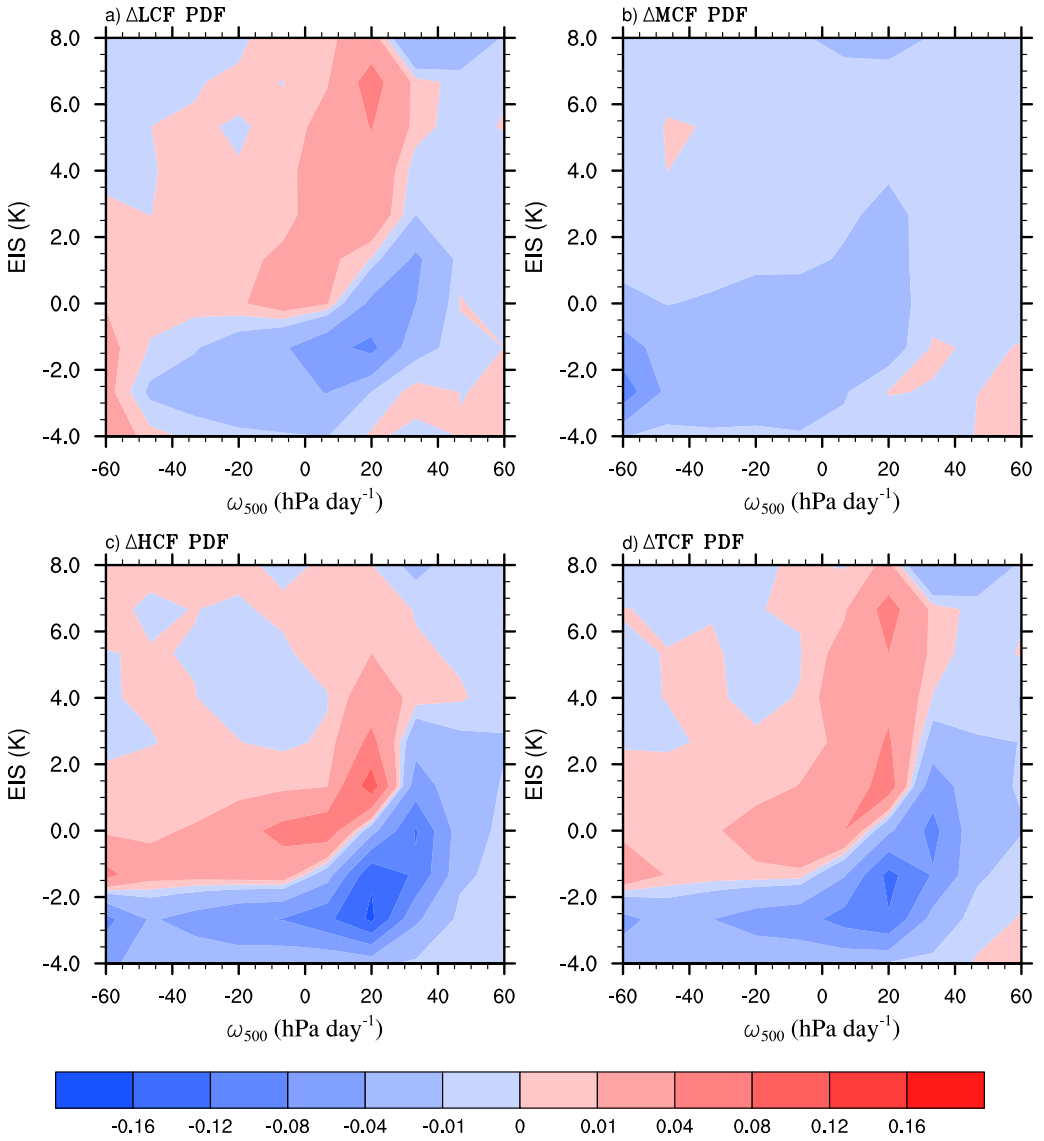

Figure 9. Similar to Figure 7 except for the thermodynamic changes. Note that the interval of the color bar is a factor of 5 smaller than that in Figure 7.

(Figures 9 and 10) are shown for the joint stability-circulation regimes. As in the circulation regime analysis, the dynamic changes are largely determined by the changes in the frequency of occurrence of the joint ω-EIS regimes (Figure 6b). The most prominent feature appears in the convective regimes (Figures 7 and 8), where the large dynamic changes for $-4 < \text{EIS} < -2$ K range are nearly canceled out by those changes for $-2 < \text{EIS} < 0$ K range. This result is related to the shift of the stability regimes as SST increases mentioned earlier. This means that the sign and magnitude of cloud feedback can be different if conventional GCMs simulate different stability changes with anthropogenic warming.

The magnitudes of the thermodynamic changes are smaller than those of the dynamic changes for the joint ω-EIS regimes. This is reflected in the color bars for Figures 9 and 10, the intervals of which are a factor of 5 smaller than those for Figures 7 and 8. The patterns of the thermodynamic changes follow those of cloud property and CRE changes between the two experiments (Figures 6c–6h) except that the magnitudes are weighted by the PDF (Figure 6a). Thus, the prior discussion on the cloud property/CRE changes is applicable to the thermodynamic changes. For the stable regimes, the thermodynamic changes are similar to those of the dynamic changes except that the shift from negative to positive cloud feedbacks occurs at 20 hPa d^{-1}

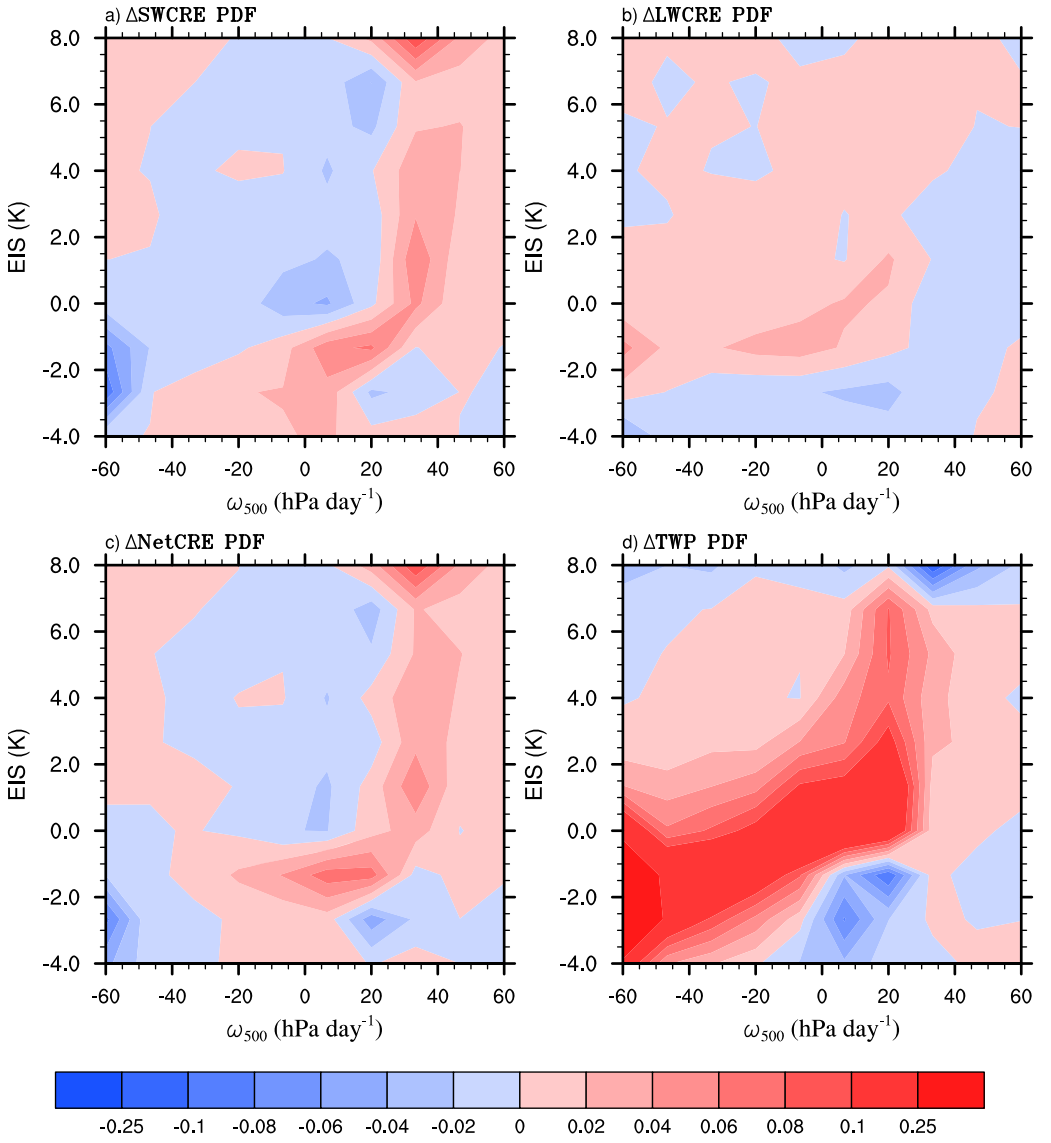

Figure 10. Similar to Figure 8 except for the thermodynamic changes. The color bar for Figure 10d is twice as large. Note that the interval of the color bar is a factor of 5 smaller than that in Figure 8.

for the thermodynamic changes (Figure 10c) but at 30 hPa d^{-1} for the dynamic changes (Figure 8c). For the unstable regimes, the net CRE thermodynamic changes vary greatly with the circulation strength (maximum positive CREs at 0–20 hPa d^{-1}; Figure 10c), as also seen from Figures 6c–6h, rather than solely with the stability strength in the dynamic changes.

The thermodynamic changes in low and high cloud fractions have different sensitivities to the stability. Both the low and high cloud fractions decrease in the moderate-to-strong subsidence regimes for nearly the entire negative EIS range. For the rest of the circulation regimes, the threshold EIS from which cloud fraction change changes sign is significantly higher for low cloud fraction than high cloud fraction (Figures 9a and 9c). The different patterns of the variations between low and high clouds, in particular, within the weak subsidence regimes, are thus important to understand cloud feedback. Note that middle clouds only impact the convective regimes (Figure 9b). These results illustrate very complicated contributions from the different cloud types to the thermodynamic changes between the two experiments in the ω-EIS space, which cannot be obtained from observational studies [e.g., *Clement et al*., 2009; *Eitzen et al*., 2011; *Myers and Norris*, 2013] or the circulation regime-only analysis.

4. Summary and Discussions

This study has examined the tropical cloud feedback from a regime sorting prospective. As revealed from studies using conventional GCMs, the thermodynamic contribution dominates the dynamic contribution to tropical cloud feedback but these models have difficulty in simulating the subsidence regimes in the tropics that lead to uncertainty in projection of future climate. In this study, we analyze the tropical cloud feedback from $+2$ K SST perturbation and control experiments performed with an upgraded MMF that is capable of realistically simulating low clouds. We sorted the monthly mean cloud and radiative properties according to the joint circulation and stability regimes and the circulation regimes only.

We found that the circulation regime-sorted dynamic change dominates the thermodynamic change in terms of the absolute magnitude although the exact magnitude of dynamic change may be more uncertain for an individual bin than for several adjacent bins that represent a wide subrange of circulation regimes. Specifically, the magnitudes of the dynamic change are much larger than those of the thermodynamic change in the weak subsidence regimes that correspond to the largest change in the power of the ω PDF. Because the sign of $\Delta P(\omega)$ changes with ω, the net contribution of the dynamic change integrated over the entire ω range is much smaller than that of the thermodynamic change for cloud fractions and LWP but slightly smaller for CREs, agreeing with previous studies [*Bony et al*., 2004; *Vial et al*., 2013]. The dynamic change exhibits negative cloud feedback for the weakly convective and weak subsidence regimes (with the largest magnitude in the weak subsidence regimes) but positive cloud feedback for the moderate-to-strong subsidence and strongly convective regimes. On the other hand, the thermodynamic change exhibits strong positive cloud feedback for the moderate-to-strong subsidence regimes and slightly negative for the weak subsidence and strongly convective regimes. The thermodynamic change in the LW CRE experiences no significant changes for all regimes and that of LW, SW, and net CREs changes little with ω in the convective regimes. Thus, the change in the SW CRE with ω in the subsidence regions plays a key role in understanding the tropical cloud feedback, agreeing qualitatively with previous studies in the sense that conventional GCMs exhibit large intermodal differences there [e.g., *Vial et al*., 2013]. Additionally, the magnitudes of dynamic contributions for high and total cloud fractions, IWP, TWP, and CREs are more comparable to those of the sums of dynamic and thermodynamic contributions. This suggests that the dynamic contribution can be important to understand cloud feedback due to its direct connection to the large-scale circulation, which was mostly ignored in some studies [e.g., *Zhao et al*., 2016].

The simulation of stratocumulus clouds and the transition between shallow and deep convection in the weak subsidence regimes are the two most critical elements to understand the tropical cloud feedback, which are poorly simulated by conventional GCMs and global cloud-resolving model [e.g., *Vial et al*., 2013; *Miura et al*., 2005]. In these regimes, shallow cumulus and deep clouds increase due to the dynamic changes. Shallow cumulus clouds increase but deep clouds decrease due to the thermodynamic changes. The dynamic changes in cloud fraction contribute strongly to the negative cloud feedback in the weak subsidence regimes, compared to the thermodynamic changes. The negative cloud feedback there is also aided by the LWP increase but the positive cloud feedback in the moderate-to-strong subsidence regimes is amplified by the LWP decrease.

The sorting approach of the joint circulation and stability regime provides further evidence of the roles of the regime transitions in contributing to the tropical cloud feedback. The power of the joint circulation-stability PDF shifts from the strong to weak subsidence regimes for the entire EIS range and from the very unstable to stable stability in the weak subsidence and convective regimes as SST increases. The latter plays a major role in determining the sign and magnitude of the dynamic changes in cloud properties and CREs when integrated over the entire EIS range. The magnitudes of the thermodynamic changes are much smaller than those of the dynamic changes and the sign of the thermodynamic changes is generally the same as that of the dynamic changes for most ω-EIS regimes. But the thermodynamic changes related to positive cloud feedback shift toward the more stable and weaker subsidence regimes, compared to that due to the dynamic changes.

This analysis illustrates very complicated contributions from low and high clouds to the thermodynamic changes in the ω-EIS space due to their different sensitivities to the stability change, especially in the weak subsidence regimes. Because of this complexity, observational studies cannot provide the full range of the stability-circulation regimes to firmly establish the sign and magnitude of cloud feedback and its

mechanisms [e.g., *Clement et al.*, 2009; *Eitzen et al.*, 2011; *Myers and Norris*, 2013; *Qu et al.*, 2015]. It is also difficult to use a single cloud feedback mechanism to explain the dynamic and thermodynamic changes. For convective regimes, the stability change plays a key role in explaining the cloud feedback mechanism. For the subsidence regimes, the circulation regime change must be the key element for any cloud-feedback mechanism because there is very little dependency of cloud feedback strength on the stability in the positive EIS range. This dependency on the circulation regime must be involved with the transitions between shallow cumulus and stratocumulus and between shallow and deep convection. The differing signs of cloud feedback are caused by either transition, which is poorly handled in conventional GCMs and earlier MMF (related to lack of stratocumulus clouds) and should be improved to quantify the cloud feedback strength. The discrepancies in the power of the circulation-regime PDFs and its change among the conventional GCMs [*Wang and Su*, 2013] are another source of uncertainty, which are critical to determine the dynamic and thermodynamic contributions to cloud feedback.

Acknowledgments
This work has been supported by DOE Atmospheric System Research Program under Interagency agreement DE-SC0005450 and DE-SC0008779. The lead author is also supported by NASA Interdisciplinary Study program. The computational resources were provided by Argonne National Laboratory, DOE's Office of Science, and the local computation clusters: K-cluster and Icluster. We thank Peter Blossey of University of Washington for providing the Matlab code to verify some of the plots and SPCAM data presented in Table 1. We thank all reviewers for their constructive comments that lead to the improvement of the final manuscript.

References

Arnold, N. P., M. Branson, M. A. Burt, D. S. Abbot, Z. Kuang, D. A. Randall, and E. Tziperman (2014), The effects of explicit atmospheric convection at high CO_2, *Proc. Natl. Acad. Sci. U. S. A.*, *111*, 10,943–10,948, doi:10.1073/pnas.1407175111.

Bengtsson, L., and S. E. Schwartz (2013), Determination of a lower bound on Earth's climate sensitivity, *Tellus, Ser. B*, *65*, 21533, doi:10.3402/tellusb.v65i0.21533.

Blossey, P. N., C. S. Bretherton, M. Zhang, A. Cheng, S. Endo, T. Heus, Y. Liu, A. P. Lock, S. R. de Roode, and K.-M. Xu (2013), Marine low cloud sensitivity to an idealized climate change: The CGILS LES intercomparison, *J. Adv. Model. Earth Syst.*, *5*, 234–258, doi:10.1002/jame.20025.

Bony, S., and J.-L. Dufresne (2005), Marine boundary layer clouds at the heart of tropical cloud feedback uncertainties in climate models, *Geophys. Res. Lett.*, *32*, L20806, doi:10.1029/2005GL023851.

Bony, S., J.-L. Dufresne, H. LeTreut, J.-J. Morcrette, and C. Senior (2004), On dynamic and thermodynamic components of cloud changes, *Clim. Dyn.*, *22*, 71–86.

Bretherton, C. S., P. N. Blossey, and C. R. Jones (2013), Mechanisms of marine low cloud sensitivity to idealized climate perturbations: A single-LES exploration extending the CGILS cases, *J. Adv. Model. Earth Syst.*, *5*, 316–337, doi:10.1002/jame.20019.

Bretherton, C. S., P. N. Blossey, and C. Stan (2014), Cloud feedbacks on greenhouse warming in the superparameterized climate model SPCCSM4, *J. Adv. Model. Earth Syst.*, *6*, 1185–1204, doi:10.1002/2014MS000355.

Cess, R. D., et al. (1990), Intercomparison and interpretation of climate feedback processes in 19 atmospheric general circulation model, *J. Geophys. Res.*, *95*, 16,601–16,615.

Cess, R. D., et al. (1996), Cloud feedback in atmospheric general circulation model: An update, *J. Geophys. Res.*, *101*, 12,791–12,794.

Cheng, A., and K.-M. Xu (2006), Simulation of shallow cumuli and their transition to deep convective clouds by cloud-resolving models with different third-order turbulence closures, *Q. J. R. Meteorol. Soc.*, *132*, 359–382.

Cheng, A., and K.-M. Xu (2008), Simulation of boundary-layer cumulus and stratocumulus clouds using a cloud-resolving model with low and third-order turbulence closures, *J. Meteorol. Soc. Jpn.*, *86A*, 67–86.

Cheng, A., and K.-M. Xu (2009), A PDF-based cloud microphysical parameterization for simulation of drizzling boundary-layer clouds, *J. Atmos. Sci.*, *66*, 2317–2334, doi:10.1175/2009JAS2944.1.

Cheng, A., and K.-M. Xu (2011), Improved low-cloud simulation from a multiscale modeling framework with a third-order turbulence closure in its cloud-resolving model component, *J. Geophys. Res.*, *116*, D14101, doi:10.1029/2010JD015362.

Cheng, A., and K.-M. Xu (2013a), Improving low-cloud simulation from an upgraded multiscale modeling framework model, Part III: Tropical and subtropical cloud transitions over the northern Pacific, *J. Clim.*, *26*, 5761–5781.

Cheng, A., and K.-M. Xu (2013b), Diurnal variability of low clouds in the southeast Pacific simulated by an upgraded multiscale modeling framework model, *J. Geophys. Res.*, *118*, 9191–9208, doi:10.1002/jgrd.50683.

Cheng, A., and K.-M. Xu (2014), An explicit representation of vertical momentum transport in a multiscale modeling framework through its 2D cloud-resolving model component, *J. Geophys. Res.*, *119*, 2356–2374, doi:10.1002/2013JD021078.

Cheng, A., K.-M. Xu, and J.-C. Golaz (2004), The liquid-water oscillation in modeling boundary-layer cumuli with third-order turbulence closure models, *J. Atmos. Sci.*, *61*, 1621–1629.

Christensen, M. W., G. Carrio, G. L. Stephens, and W. R. Cotton (2013), Radiative impacts of free-tropospheric clouds on the properties of marine stratocumulus, *J. Atmos. Sci.*, *70*, 3102–3118, doi:10.1175/JAS-D-12-0287.1.

Clement, A. C., and B. Soden (2005), The sensitivity of the tropical-mean radiation budget, *J. Clim.*, *18*, 3189–3203.

Clement, A. C., R. Burgman, and J. R. Norris (2009), Observational and model evidence for positive low-level cloud feedback, *Science*, *325*, 460–464, doi:10.1126/science.1171255.

Collins, W. D., et al. (2006), The formulation and atmospheric simulation of the Community Atmosphere Model Version 3 (CAM3), *J. Clim.*, *19*, 2144–2161.

Colman, R., J. Fraser, and L. Rotstayn (2001), Climate feedbacks in a general circulation model incorporating prognostic clouds, *Clim. Dyn.*, *18*, 103–122.

Demoto, S., M. Watanabe, and Y. Kamae (2013), Mechanism of tropical low-cloud response to surface warming using weather and climate simulation, *Geophys. Res. Lett.*, *40*, 2427–2432, doi:10.1002/grl.50474.

Eitzen, Z. A., K.-M. Xu, and T. Wong (2011), An estimate of low-cloud feedbacks from variations of cloud radiative and physical properties with sea surface temperature on interannual time scales, *J. Clim.*, *24*, 1106–1121, doi:10.1175/2010JCLI3670.1.

Feigelson, E. M. (1978), Preliminary radiation model of a cloudy atmosphere, 1, Structure of clouds and solar radiation, *Contrib. Atmos. Phys.*, *51*, 203–229.

Golaz, J.-C., V. E. Larson, and W. R. Cotton (2002), A PDF-based model for boundary layer clouds. Part I: Method and model description, *J. Atmos. Sci.*, *59*, 3540–3551.

Grabowski, W. W. (2001), Coupling cloud processes with the large-scale dynamics using the cloud-resolving convection parameterization (CRCP), *J. Atmos. Sci.*, *58*, 978–997.

Hansen, J., A. Lacis, D. Rind, G. Russell, P. Stone, I. Fung, R. Ruedy, and J. Lerner (1984), Climate sensitivity: Analysis of feedback mechanisms, in *Climate Processes and Climate Sensitivity, Geophys. Monogr. Ser.*, vol. 29, edited by J. E. Hansen and T. Takahashi, pp. 130–163, AGU, Washington, D. C.

He, J., and B. J. Soden (2015), Anthropogenic weakening of the tropical circulation: The relative roles of direct CO_2 forcing and sea surface temperature change, *J. Clim.*, *28*, 8728–8742, doi:10.1175/JCLI-D-15-0205.1.
Kato, S., et al. (2011), Improvements of top-of-atmosphere and surface irradiance computations with CALIPSO, CloudSat, and MODIS-derived cloud and aerosol properties, *J. Geophys. Res.*, *116*, D19209, doi:10.1029/2011JD016050.
Khairoutdinov, M. F., and D. A. Randall (2001), A cloud resolving model as a cloud parameterization in the NCAR community climate system model: Preliminary results, *Geophys. Res. Lett.*, *28*, 3617–3620.
Khairoutdinov, M. F., D. A. Randall, and C. A. DeMott (2005), Simulations of the atmospheric general circulation using a cloud-resolving model as a superparameterization of physical processes, *J. Atmos. Sci.*, *62*, 2136–2154, doi:10.1175/JAS3453.1.
Mauritsen, T., and B. Stevens (2015), Missing iris effect as a possible cause of muted hydrological change and high climate sensitivity in models, *Nat. Geosci.*, *8*, 345–351, doi:10.1038/ngeo2414.
Medeiros, B., B. Stevens, I. M. Held, M. Zhao, D. L. Williamson, J. G. Olson, and C. S. Bretherton (2008), Aquaplanets, climate sensitivity, and low clouds, *J. Clim.*, *21*, 4974–4991, doi:10.1175/2008JCLI1995.1.
Medeiros, B., B. Stevens, and S. Bony (2015), Using aquaplanets to understand the robust responses of comprehensive climate models to forcing, *Clim. Dyn.*, *44*, 1957–1977, doi:10.1007/s00382-014-2138-0.
Miura, H., H. Tomita, T. Nasuno, S. Iga, M. Satoh, and T. Matsuno (2005), A climate sensitivity test using a global cloud resolving model under an aqua planet condition, *Geophys. Res. Lett.*, *32*, L19717, doi:10.1029/2005GL023672.
Myers, T. A., *and* J. R. Norris (2013), Observational evidence that enhanced free-tropospheric subsidence reduces marine boundary layer cloudiness, *J. Clim.*, *26*, 7507–7524, doi:10.1175/JCLI-D-12-00736.1.
Myhre, G., E. J. Highwood, K. P. Shine, and F. Stordal (1998), New estimates of radiative forcing due to well mixed greenhouse gases, *Geophys. Res. Lett.*, *25*, 2715–2718, doi:10.1029/98GL01908.
Painemal, D., K.-M. Xu, A. Cheng, P. Minnis, and R. Palikonda (2015), Mean structure and diurnal cycle of southeast Atlantic boundary layer clouds: Insights from satellite observations and multiscale modeling framework simulations, *J. Clim.*, *28*, 324–341.
Paltridge, G. W. (1980), Cloud-radiation feedback to climate, *Q. J. R. Meteorol. Soc.*, *106*, 895–899.
Qu, X., A. Hall, S. A. Klein, and P. M. Caldwell (2014), On the spread of changes in marine low cloud cover in climate model simulations of the 21st century, *Clim. Dyn.*, *42*, 2603–2626, doi:10.1007/s00382-013-1945-z.
Qu, X., A. Hall, S. A. Klein, and P. M. Caldwell (2015), The strength of the tropical inversion and its response to climate change in 18 CMIP5 models, *Clim. Dyn.*, *45*, 375–396, doi:10.1007/s00382-014-241-9.
Ramanathan, V., R. D. Cess, E. F. Harrison, P. Minnis, B. R. Barkstrom, E. Ahmad, and D. Hartmann (1989), Cloud-radiative forcing and climate: Results from the Earth Radiation Budget Experiment, *Science*, *243*, 57–63.
Randall, D. A., et al. (2003), Confronting models with data: The GEWEX Cloud Systems Study, *Bull. Am. Meteorol. Soc.*, *84*, 455–469, doi:10.1175/BAMS-84-4-455.
Randall, D. A., et al. (2007), Climate models and their evaluation, in *Climate Change 2007: The Physical Science Basis. Contribution of Working Group I to the Fourth Assessment Report of the Intergovernmental Panel on Climate Change*, pp. 589–662, Cambridge Univ. Press, Cambridge, U. K.
Rayner, N. A., D. E. Parker, E. B. Horton, C. K. Folland, L. V. Alexander, D. P. Rowell, E. C. Kent, and A. Kaplan (2003), Global analyses of sea surface temperature, sea ice, and night marine air temperature since the late nineteenth century, *J. Geophys. Res.*, *108*(D14), 4407, doi:10.1029/2002JD002670.
Ringer, M. A., et al. (2006), Global mean cloud feedbacks in idealized climate change experiments, *Geophys. Res. Lett.*, *33*, L07718, doi:10.1029/2005GL025370.
Ringer, M. A., T. Andrews, and M. J. Webb (2014), Global-mean radiative feedbacks and forcing in atmosphere-only and coupled atmosphere-ocean climate change experiments, *Geophys. Res. Lett.*, *41*, 4035–4042, doi:10.1002/2014GL060347.
Schneider, S. H. (1972), Cloudiness as a global climatic feedback mechanism: The effects on radiation balance and surface-temperature of variations in cloudiness, *J. Atmos. Sci.*, *29*, 1413–1422.
Soden, B. J., and G. A. Vecchi (2011), The vertical distribution of cloud feedback in coupled ocean-atmosphere models, *Geophys. Res. Lett.*, *38*, L12704, doi:10.1029/2011GL047632.
Stan, C., and L. Xu (2014), Climate simulations and projections with the super-parameterized CCSM4, *Environ. Model. Software*, *60*, 1234–252, doi:10.1016/j.envsoft.2014.06.013.
Stephens, G. L. (2005), Cloud feedbacks in the climate systems: A critical review, *J. Clim.*, *18*, 237–273, doi:10.1075/JCLI-3243.1.
Taylor, K. E., R. J. Stouffer, and G. A. Meehl (2012), An overview of CMIP5 and the experiment design, *Bull. Am. Meteorol. Soc.*, *93*, 485–498, doi:10.1175/BAMS-D-11-00094.1.
Vecchi, G. A., and B. J. Soden (2007), Global warming and the weakening of the tropical circulation, *J. Clim.*, *20, 41*, 4316–4340, doi:10.1175/JCLI4258.1.
Vial, J., J.-L. Dufresne, and S. Bony (2013), On the interpretation of inter-model spread in CMIP5 climate sensitivity estimates, *Clim. Dyn.*, 3339–3362, doi:10.1007/s00382-013-1725-9.
Wang, H., and W. Su (2013), Evaluating and understanding top of the atmosphere cloud radiative effects in Intergovernmental Panel on Climate Change (IPCC) Fifth Assessment Report (AR5) Coupled Model Intercomparison Project Phase 5 (CMIP5) models using satellite observations, *J. Geophys. Res.*, *118*, 683–699, doi:10.1029/2012JD018619.
Wang, L., Y. Wang, A. Lauer, and S.-P. Xie (2011), Simulation of seasonal variation of marine boundary layer clouds over the eastern Pacific with a regional climate model, *J. Clim.*, *24*, 3190–3210.
Wang, M., V. E. Larson, S. Ghan, M. Ovchinnikov, D. P. Schanen, H. Xiao, X. Liu, P. Rasch, and Z. Guo (2015), A multi-scale modeling framework model (super-parameterized CAM5) with a higher-order turbulence closure: Model description and low cloud simulations. *J. Adv. Model. Earth Syst.*, *7*, 484–509, doi:10.1002/2014MS000375.
Wetherald, R. T., and S. Manabe (1980), Cloud cover and climate sensitivity, *J. Atmos. Sci.*, *37*, 1485–1510.
Wielicki, B. A., B. R. Barkstrom, E. F. Harrison, R. B. Lee, G. L. Smith, and J. E. Cooper (1996), Clouds and the Earth's Radiant Energy System (CERES): An Earth Observing System experiment, *Bull. Am. Meteorol. Soc.*, *77*, 853–868.
Wilks, D. S. (2006), *Statistical Methods in the Atmospheric Sciences*, 2nd ed., 627 pp., Academic, Burlington, Mass.
Wood, R., and C. S. Bretherton (2006), On the relationship between stratiform low cloud cover and lower-tropospheric stability, *J. Clim.*, *19*, 6425–6432.
Wyant, M. C., M. Khairoutdinov, and C. S. Bretherton (2006a), Climate sensitivity and cloud response of a GCM with a superparameterization, *Geophys. Res. Lett.*, *33*, L06741, doi:10.1029/2005GL025464.

Wyant, M. C., C. S. Bretherton, J. T. Bacmeister, J. T. Kiehl, I. M. Held, M. Zhao, S. A. Klein, and B. J. Soden (2006b), A comparison of low-latitude cloud properties and their response to climate change in three AGCMs sorted into regimes using mid-tropospheric vertical velocity, *Clim. Dyn.*, *27*, 261–279, doi:10.1007/s00382-006-0138-4.

Wyant, M. C., et al. (2010), The preVOCA experiment: Modeling the lower troposphere in the southeast Pacific, *Atmos. Chem. Phys.*, *10*, 4757–4774, doi:10.5194/acp-10-4757-2010.

Wyant, M. C., C. S. Bretherton, P. N. Blossey, and M. Khairoutdinov (2012), Fast cloud adjustment to increasing CO_2 in a superparameterized climate model, *J. Adv. Model. Earth Syst.*, *4*, M05001, doi:10.1029/2011MS000092.

Xu, K.-M., and A. Cheng (2013a), Improving low-cloud simulation from an upgraded multiscale modeling framework model, Part I: Sensitivity to spatial resolution and climatology, *J. Clim.*, *26*, 5717–5740.

Xu, K.-M., and A. Cheng (2013b), Improving low-cloud simulation from an upgraded multiscale modeling framework model, Part II: Seasonal variations over the eastern Pacific, *J. Clim.*, *26*, 5741–5760.

Xu, K.-M., A. Cheng, and M.-H. Zhang (2010), Cloud-resolving simulation of low-cloud feedback to an increase in sea surface temperature, *J. Atmos. Sci.*, *67*, 730–748.

Yuan, J., D. L. Hartmann, and R. Wood (2008), Dynamic effects on the tropical cloud radiative forcing and radiation budget, *J. Clim.*, *21*, 2337–2351.

Yukimoto, S., A. Noda, A. Kitho, M. Hoasaka, H. Yoshimura, T. Uchiyama, K. Shibata, O. Arakawa, and S. Kusunoki (2006), Present-day climate and climate sensitivity in the Meteorological Research Institute coupled GCM version 2.3 (MRI-CGCM2.3), *J. Meteorol. Soc. Jpn.*, *84*(2), 333–363, doi:10.2151/jmsj.84.333.

Zhao, M., J.-C. Golaz, I. M. Held, V. Ramaswamy, S.-J. Lin, Y. Ming, P. Ginoux, B. Wyman, L. J. Donner, D. Paynter, and H. Guo (2016), Uncertainty in model climate sensitivity traced to representations of cumulus precipitation microphysics, *J. Clim.*, *29*, 543–560, doi:10.1175/JCLI-D-15-0191.1.